https://doi.org/10.5194/bg-2020-254
Preprint. Discussion started: 16 July 2020

Biogeosciences Discussions

Ocean Carbon Uptake Under Aggressive Emission Mitigation

Sean Ridge[1] and Galen McKinley[1]

[1]Lamont-Doherty Earth Observatory of Columbia University, P.O. Box 1000, 61 Route 9W, Palisades, NY

Correspondence: Sean Ridge (sridge@ldeo.columbia.edu)

Abstract. Nearly every nation has signed the UNFCC Paris Agreement, committing to mitigate global anthropogenic carbon (C_{ant}) emissions and limit global mean temperature increase to 1.5°C. A consequence of emission mitigation is reduced efficiency of ocean C_{ant} uptake, which is driven by mechanisms that have not been studied in detail. The historical pattern of continual increase in atmospheric CO_2 has resulted in a proportional increase in C_{ant} uptake. Here, we explore how this proportionality will weaken and find significant effects related to changes in the vertical transfer of C_{ant} from the surface to the deep ocean, and also ocean chemistry. We define ocean uptake growth consistent with an exact proportionality to the atmospheric growth rate, i.e. the historical scaling, to be 100% efficient. Using a model hierarchy consisting of a commonly used one-dimensional ocean carbon cycle model and a complex Earth System Model (ESM), we find that declines in the efficiency of ocean uptake are greatest under aggressive emission mitigation. To understand the drivers of efficiency declines, we use the ESM to compare scenarios with aggressive emission mitigation (1.5°C), intermediate emission mitigation (RCP4.5), and no emission mitigation (RCP8.5). Using the one-dimensional ocean carbon cycle model, we demonstrate how growth of ocean C_{ant} uptake is a balance between enhancement due to a positive atmospheric CO_2 growth rate, and decreases due to the positive growth rate of dissolved CO_2 in the surface ocean. Without emission mitigation (RCP8.5), changes in efficiency are almost entirely the result of changes in the buffer capacity of the ocean, which accelerates the growth rate of dissolved CO_2 in the surface ocean. Under the declining CO_2 regime of the 1.5°C scenario, the dominant driver of efficiency decline is the carbon gradient effect, wherein C_{ant} in the ocean interior slows the removal of C_{ant} from the surface. Although the carbon gradient effect is an unavoidable consequence of emission mitigation, it can be reduced by hastily pursuing emission mitigation.

1 Introduction

The ocean has absorbed 39% of the CO_2 from industrial era fossil fuel combustion and cement production (Friedlingstein et al., 2019). The rest of the CO_2 remains in the atmosphere where it acts as the primary driver of climate change. At the global scale, the partial pressure of CO_2 in the atmosphere (pCO_2^{atm}) is greater than the partial pressure of CO_2 in the surface ocean (pCO_2^{ocn}), thus there is a net ocean sink. The difference in partial pressures has grown over time, therefore ocean uptake of atmospheric CO_2 has increased over the industrial era (Khatiwala et al., 2009; DeVries, 2014). The carbon that has been added to the ocean and atmosphere as the result of anthropogenic CO_2 emissions is referred to as anthropogenic carbon, C_{ant}.

https://doi.org/10.5194/bg-2020-254
Preprint. Discussion started: 16 July 2020


Biogeosciences Discussions Open Access EGU

The rate of ocean C_{ant} uptake is controlled by the rate of physical removal of C_{ant} from the surface ocean into the ocean interior. Various processes set the rate of physical C_{ant} removal, with significant contributions coming from vertical diapycnal diffusion and isopycnal eddy diffusion (Bopp et al., 2015; Gnanadesikan et al., 2015). Advection dominates regional patterns C_{ant} fluxes into (reemergence) and out of (subduction) the seasonal mixed layer (Bopp et al., 2015; Toyama et al., 2017). The large positive and negative signs of the advective flux mostly cancel when globally integrated (Bopp et al., 2015), thus advection does not play a dominant role in setting the globally integrated C_{ant} air-sea flux. In density space, C_{ant} is primarily absorbed in lighter subtropical waters, and then transferred to denser mode and intermediate waters by diapycnal fluxes associated with watermass transformation (Iudicone et al. 2016). Using an effective surface diffusivity ($K_{z,eff}$), i.e. summarizing the net removal by these processes as a single diffusive process, one-dimensional diffusion models have been shown to be consistent with observations and complex models (Gnanadesikan et al., 2015; Oeschger et al., 1975).

Growth of the natural sinks (land biosphere and ocean) has been outpaced by the growth of atmospheric CO_2 and thus sink efficiency has declined (Canadell et al., 2007; Raupach et al., 2014). Efficiency of land and ocean sinks is described by the CO_2 sink rate (k_S; Raupach et al., 2014), which is the combined ocean-land CO_2 uptake per unit atmospheric CO_2 above preindustrial levels ($C_{ant,A}$; Pg C):

$$k_S(t) = \frac{F_{ant,L}(t) + F_{ant,M}(t)}{C_{ant,A}(t)} \quad (1)$$

Where $F_{ant,L}$ (Pg C yr^{-1}) is the anthropogenic land sink and $F_{ant,M}$ (Pg C yr^{-1}) is the anthropogenic ocean sink. Observations of k_S from 1959-2012 indicate a robust declining trend, and thus the rate of increase in the natural sinks was slower than the accumulation of carbon in the atmosphere. Using a simple climate model, Raupach et al. (2014) attribute the declining trend to slower-than-exponential CO_2 emissions growth ($\sim$35% of the trend), a decline in the size of major volcanic eruptions, which cause brief periods of global cooling ($\sim$25%), response of the natural sinks to a warming climate ($\sim$20%), and nonlinear responses to increasing atmospheric CO_2 (mostly attributable to ocean chemistry; $\sim$20%).

Slowing of the emissions growth rate, and thus the pCO_2^{atm} growth rate, reduces the efficiency of ocean C_{ant} uptake (McKinley et al., 2020; Raupach et al., 2014); this response is related to the timescales of C_{ant} transfer to the ocean interior (Raupach et al. 2014). A reduced pCO_2^{atm} growth rate is inevitable, due either to climate policy, or by the eventual exhaustion of fossil fuel reservoirs. Nearly every nation has signed the Paris Agreement, which requires participating governments to pledge to mitigate future greenhouse gas emissions in an attempt to limit the global mean temperature increase to 1.5°C. While countries' emissions pledges are incompatible with the 1.5°C goal (UNEP, 2019), continued commitment to these emissions pledges will inevitably end the historical pattern of exponential pCO_2^{atm} growth in coming decades.

The reductions to efficiency that are attributable to a slowing pCO_2^{atm} growth rate will be at least partially compensated by a decrease in the strength of the climate-carbon feedbacks that reduce efficiency of ocean C_{ant} uptake (Friedlingstein et al., 2013; Raupach et al., 2014). Past studies have separated carbon cycle feedbacks into CO_2 concentration effects and climate driven effects (Friedlingstein et al., 2013). The CO_2 concentration driven effect is the net result of two effects: increased flux driven by increasing pCO_2^{atm} and reduced flux driven by a declining buffer capacity of the ocean. The buffering capacity of

https://doi.org/10.5194/bg-2020-254
Preprint. Discussion started: 16 July 2020


Biogeosciences Discussions Open Access EGU

the ocean refers to the transfer of absorbed CO_2 via chemical reactions into chemical species that do not exchange with the atmosphere. As more CO_2 is added to the ocean, buffer capacity decreases (Fassbender et al., 2017). When buffer capacity is reduced, more of the CO_2 remains in a form that can exchange with the atmosphere and the efficiency of ocean C_{ant} uptake declines.

Climate driven effects stem from the warming of the surface ocean, which impacts gas solubility and ocean circulation. Projected warming reduces ocean uptake (Friedlingstein et al., 2013) and thus reduces the efficiency of ocean uptake . This impact of warming on future carbon uptake has been quantified using a climate feedback framework (Friedlingstein et al., 2013; Randerson et al., 2015; Schwinger and Tjiputra, 2018). However, the idealized simulations used in these studies have not allowed for quantification of the additional contribution of reduced buffering capacity to reduced ocean carbon uptake.

This work expands upon previous work that has quantified future change in ocean C_{ant} uptake by separately accounting for changes due to buffering. We will compare a future scenario with moderate levels of mitigation (RCP4.5; Meinshausen et al., 2011), and an aggressive mitigation scenario where the 1.5°C target is met (1.5°C; Sanderson et al., 2017) to RCP8.5 using an Earth System model (ESM). In the RCP8.5 scenario (Meinshausen et al., 2011), pCO_2^{atm} increases exponentially and represents our no mitigation baseline. With our set of ocean carbon cycle simulations, we will calculate how warming and reduced buffering, referred to here as chemical capacity, affect ocean C_{ant} uptake.

The contribution of ocean C_{ant} uptake to k_S is referred to as k_M:

$$k_M(t) = \frac{F_{ant,M}(t)}{C_{ant,A}(t)} \tag{2}$$

In the past, k_M has been influenced by a slowing of the CO_2 emissions growth rate (McKinley et al., 2020), volcanic aerosol induced cooling of the surface ocean (McKinley et al., 2020), changing ocean chemistry, and changes to physical climate (Friedlingstein et al., 2013).

Under exponentially increasing pCO_2^{atm}, constant gas solubility, and constant chemical capacity, k_M, would remain constant, and thus by definition, the proportionality between increases in atmospheric CO_2 and increases in ocean C_{ant} uptake would also remain constant. Because these conditions approximately describe the historical conditions of the ocean carbon cycle, constant proportionality for ocean C_{ant} uptake has been used as a null hypothesis in studies of the drivers of historical regional and global scale changes in the ocean carbon cycle (Lovenduski et al., 2008; Gruber et al., 2019a). Here we refer to this constant proportionality (i.e. $k_M = constant$) as the "historical scaling", instead of the seemingly contradictory original term, the "transient steady state assumption" (Gammon et al., 1982; Tanhua et al., 2007; Lovenduski et al., 2008; Gruber et al., 2019a). With constant k_M, the evolution of ocean C_{ant} concentration at all points in space also follows the historical scaling. This is because the exponential shape of pCO_2^{atm} is passed on to pCO_2^{ocn} by the C_{ant} air-sea flux. The amplifying effect that approximately exponentially increasing pCO_2^{atm} has on the ocean C_{ant} concentration and ocean C_{ant} uptake can be removed using the historical scaling, and in previous work, deviations from the historical scaling for ocean C_{ant} uptake and C_{ant} concentrations have been attributed entirely to internal ocean mechanisms. However, we illustrate that previous work has likely overestimated of the impacts of internal variability on the ocean carbon cycle, given the close relationship between the histor-

https://doi.org/10.5194/bg-2020-254
Preprint. Discussion started: 16 July 2020

ical scaling and k_M, which is sensitive external mechanisms such as volcanic forcings and pCO_2^{atm} growth rate (McKinley et al., 2020).

The focus of this work is to determine the primary mechanisms in projections of future climate that will drive reductions to the efficiency of ocean C_{ant} uptake under emission mitigation and, thus, a reduced growth rate of atmospheric CO_2. Here we consider efficiency of ocean C_{ant} uptake as a measure of how effectively the input, pCO_2^{atm}, is converted into the desired output, ocean C_{ant} uptake. More efficient ocean C_{ant} uptake would result in the ocean absorbing more carbon at a given pCO_2^{atm}. In the following sections, we use a one-dimensional ocean carbon cycle model to diagnose the mechanisms of efficiency decline in climate projections from a complex ESM, with the goal of understanding future changes in the efficiency of ocean C_{ant} uptake.

2 Methods

In this section, we develop equations for ocean sink efficiency and introduce our one-dimensional ocean carbon cycle model. We identify the mechanisms driving changes in efficiency by comparing the behaviour of a one-dimensional ocean carbon cycle model to an ESM, the Community Earth System Model (CESM). CESM simulations are publicly available, provided by the National Center for Atmospheric Research (NCAR). The one-dimensional ocean carbon cycle model emulates the ocean circulation and carbon cycling of the ESM, but allows for rapid integration to facilitate mechanistic exploration.

2.1 Efficiency Metric and Historical Scaling

Ocean sink rate (k_M; Equation 2) represents the efficiency of ocean C_{ant} uptake. The efficiency metric used here, η, is k_M referenced to the year 1990, so that efficiency may be expressed as a percentage:

$$\eta(t) = \frac{k_M(t)}{k_M(1990)} \times 100 \tag{3}$$

Referencing k_M to 1990 values maximizes the time ocean C_{ant} uptake is at 100% efficiency during the historical period, 1920-2006 (Figure S1). The historical scaling for ocean C_{ant} uptake (F_{ant}) is closely related to k_M :

$$\overset{*}{F}_{ant}(t) = k_M(1990) C_{ant,A}(t) = F_{ant}(1990) \frac{C_{ant,A}(t)}{C_{ant,A}(1990)} \tag{4}$$

The rightmost expression in Equation 4 is the F_{ant} historical scaling, and is based the assumption of constant efficiency, and thus mathematically equivalent to extrapolating F_{ant} using a fixed k_M (Equation 2,4). The overset "*" notation indicates the variable that has been extrapolated with the historical scaling. When using the historical scaling, $F_{ant}(1990)$ is diagnosed from the CESM, and $\overset{*}{F}_{ant}(t)$ is obtained mathematically by extrapolating $F_{ant}(1990)$ based on the relative increase in atmospheric C_{ant} from 1990 values ($\frac{C_{ant,A}(t)}{C_{ant,A}(1990)}$). For example, $F_{ant}(1990)$ simulated by CESM was 1.7 Pg C_{ant} yr^{-1}, and the atmospheric perturbation in 1990 was 74 ppm (∼157 Pg C). In the future, if the atmospheric perturbation is doubled from 1990

https://doi.org/10.5194/bg-2020-254
Preprint. Discussion started: 16 July 2020

values to 148 ppm (∼314 Pg C), $\overset{*}{F}_{ant}$ would also double to 3.4 Pg C_{ant} yr^{-1}. Expressing ocean carbon sink efficiency (η) as Equation 5 illustrates the link to the historical scaling:

$$\eta(t) = \frac{F_{ant}(t)}{\overset{*}{F}_{ant}(t)} \times 100 \tag{5}$$

Equation 5 is equivalent to Equation 3, and is obtained by expanding Equation 3 into terms of F_{ant} and $C_{ant,A}$. Under the approximately exponential pCO_2^{atm} increase of the historical period, k_M is relatively constant, thus $F_{ant}(t) \approx \overset{*}{F}_{ant}(t)$ and historical period efficiency is ∼100%. Because it is approximately equal to F_{ant}, $\overset{*}{F}_{ant}$ has been used by biogeochemical oceanographers to estimate historical $F_{ant}(t)$ (Lovenduski et al., 2008). In the future, as k_M declines from 1990 values, F_{ant} will be less than $\overset{*}{F}_{ant}(t)$, and efficiency will decline. Here $\overset{*}{F}_{ant}(t)$, extrapolated into the future with projected pCO_2^{atm}, will be used to represent an upper bound for future ocean C_{ant} uptake.

While k_M remains constant, the global mean ocean C_{ant} profile ($C_{ant}(z,t)$) can also be estimated ($\overset{*}{C}_{ant}(z,t)$) using the historical scaling (Tanhua et al., 2007; Gruber et al., 2019a):

$$\overset{*}{C}_{ant}(z,t) = C_{ant}(z,1990)\frac{C_{ant,A}(t)}{C_{ant,A}(1990)} \tag{6}$$

The C_{ant} historical scaling exists because the C_{ant} air-sea flux is effectively "pulling" pCO_2^{ocn} towards pCO_2^{atm}, so under the observed exponentially increasing pCO_2^{atm}, pCO_2^{ocn} and pCO_2^{atm} are both exponential curves. Because ocean chemistry has remained relatively constant over the historical period, we have been able to assume that surface ocean C_{ant} concentration is linearly related to pCO_2^{ocn}. Mathematically, surface ocean C_{ant} concentration is closely related to the time integral of the C_{ant} air-sea flux (Methods 2.3). Therefore, because the integral of an exponential is also an exponential, surface C_{ant} concentration has also increased exponentially, and that exponential is then propagated by ocean circulation to deeper layers. However, looking forward, the linear relationship between C_{ant} concentration and pCO_2^{ocn} will end due to a decreasing chemical capacity for CO_2. Also, the propagation of the surface exponential signal to depth by ocean circulation is not instantaneous, thus when emissions are mitigated, waters towards the surface will be changing in proportion to flattening atmospheric CO_2 , but deeper in the water column they will be changing in proportion to the exponential atmospheric CO_2 signal from decades prior. Future $C_{ant}(z)$, will deviate from $\overset{*}{C}_{ant}(z)$.

2.2 Ocean Component of the Earth System Model

The CESM provides a realistic simulation of the response of the ocean carbon cycle to climate change. The CESM's ocean component model, POP2, provides the ocean biogeochemistry output analyzed in sections 3.1 and 3.2. POP2 output is from publicly available CESM climate simulations provided by NCAR. POP2 features 60 vertical levels and a nominal 1° x 1° horizontal resolution. Surface boundary layer physics are parameterized using the K-Profile Parameterization (KPP) of Large et al. (1994). Unresolved advection by eddies is parameterized with the Gent-McWilliams parameterization (1990). Isopycnal mixing is parameterized with the Redi (1982) diffusion operator. The biogeochemical output comes from the embedded

https://doi.org/10.5194/bg-2020-254
Preprint. Discussion started: 16 July 2020

Biogeochemical Elemental Cycle (BEC) model (Moore et al., 2004). C_{ant} concentration is calculated in the model as the difference between natural carbon (C_{nat}), a tracer that experiences a fixed preindustrial pCO_2^{atm}, and contemporary carbon (C_{con}), a tracer that experiences time evolving pCO_2^{atm}.

All of the climate simulations used here are forced with pCO_2^{atm} from the Representative Concentration Pathways (RCPs) or a 1.5°C scenario (Sanderson et al., 2017) from 2006-2080. Over the historical period, 1920-2005, these simulations are forced with observations of pCO_2^{atm}. For the 1.5°C scenario, a concentration pathway was designed that limited warming the CESM to 1.5°C, for the purpose of investigating avoided climate impacts (Sanderson et al., 2017). This scenario features the same forcing as RCP8.5 until 2017, except for CO_2. The projected CO_2 forcing was not smoothly joined to the historical CO_2 forcing, creating a period of low C_{ant} flux, which the ocean C_{ant} sink recovers from by 2017 (Figure S2).

Multiple simulations are run with the same pCO_2^{atm} forcing to generate single model ensembles for each scenario. The ensemble approach allows for separation of internal variability from the forced signals, with the latter being the focus of this study. NCAR has run multiple ensembles with different forcings including CESM Large Ensemble (40 members, RCP8.5; Kay et al. 2014), CESM Medium Ensemble (15 members, RCP4.5), and the CESM Low-Warming Ensemble (10 members, 1.5°C; Sanderson et al., 2017). Ocean biogeochemistry output is limited to 9 members for the medium ensemble and the 3 for the low warming ensemble, thus we also only use 9 ensemble members for the RCP8.5 experiment.

In coupled climate models, historical climate variability of the carbon sink is not expected to match observations because the phasing of ENSO or other internal climate variability is different in each ensemble member. Averaging across an ensemble removes the imprint of internal variability leaving only the climate system response to external forcing. With only a single coupled climate simulation, decadal means are used to smooth internal climate variability, but with an ensemble, a single year of the ensemble mean provides a snapshot of the climate response to external forcing. All output analyzed here is the ensemble mean because we are focused on the externally forced signal. CESM is used for maps and sections, and we tune a one-dimensional model to replicate its global mean behavior to elucidate the underlying mechanisms.

2.3 One-Dimensional Ocean Carbon Cycle Model

The behavior of the one-dimensional ocean carbon cycle model is more easily interpreted than the behavior of the complex ESM. Here we employ an established one-dimensional ocean carbon cycle model that is based on impulse response functions. This model is easily interpretable and has been used for decades to emulate ocean carbon uptake simulated by complex ESMs (Joos et al., 1996; Meinshausen et al., 2011; Raupach et al., 2014). The impulse response function form of our model has been used to convert emissions projections into the CO_2 concentration pathways (RCP4.5, RCP8.5) that are used to force the CESM, as well as others in the CMIP5 suite of ESMs (Meinshausen et al., 2011) used in IPCC AR5 (Cias et al., 2013).

Impulse response functions can be used to characterize the response of dynamical systems to small perturbations around a steady state. In our case, the small perturbation is the C_{ant} perturbation to the preindustrial carbon cycle. With this method, the full response of the system is considered to be the sum of the system's response to infinitely many discrete pulses. For the ocean carbon cycle, a pulse is the C_{ant} added to the surface ocean by air-sea exchange for a time frame specified by the one-dimensional model's time step. The impulse response function describes how long that C_{ant} pulse remains in surface ocean.

https://doi.org/10.5194/bg-2020-254
Preprint. Discussion started: 16 July 2020

C_{ant} air-sea flux and surface C_{ant} concentration are calculated at each time step, while the response function is fixed. The surface ocean C_{ant} is mathematically expressed as the convolution integral of the impulse (C_{ant} air-sea flux) and the impulse response function (lifetime of that C_{ant} pulse). A conceptual version of this approach is illustrated in Appendix A.

The one-dimensional model is forced with the same historical and projected pCO_2^{atm} that is used to force the ocean component of the ESM, and historical and projected SST change simulated by the ocean component of ESM. With this one-dimensional model we can calculate the annual mean C_{ant} concentration and the globally integrated C_{ant} air-sea flux. The one-dimensional model consists of two equations (Equation 7,10) that are solved at each timestep to obtain the air-sea flux of C_{ant}:

$$C_{ant}(t) = \frac{1}{h} \int_{t_i}^{t} F_{ant}(u) r(t-u) du \tag{7}$$

This is the convolution integral of C_{ant} air-sea flux (F_{ant}) and the mixed-layer impulse response function, $r(t)$. A convolution integral calculates the concentration at time t by calculating the fraction of previous pulses ($F_{ant}(u)$), that entered the ocean at times u (from $t_i = 0$ to t), that remain in the surface ocean at time t. The effective mixed layer depth, h, converts the output of the convolution integral into from mmol m^{-2} to units of mmol m^{-3}. We use h to tune the historical C_{ant} air-sea flux of the one-dimensional model to the historical C_{ant} air-sea flux of the ocean component of the ESM. In our case, the optimal h to match the behavior of the CESM ocean component model is 109 m.

The mixed-layer impulse response function ($r(t)$) used here is from Joos et al. (1996), and was diagnosed by those authors from the box-diffusion model, HILDA (HIgh Latitude-exchange/interior Diffusion-Advection). With this method, the response function is fixed throughout time, which is equivalent to the assumption that ocean circulation is constant.

The convolution integral (Equation 7) represents the time integral of a box-diffusion model's surface C_{ant} tendency equation:

$$\frac{\partial C_{ant}}{\partial t} = \frac{F_{ant}}{h} + \frac{K_{z,eff}}{h} \frac{\partial C_{ant}}{\partial z} \tag{8}$$

$$C_{ant}(t) = \frac{1}{h} \int_{0}^{t} \left(F_{ant} + K_{z,eff} \frac{\partial C_{ant}}{\partial z} \right) dt \tag{9}$$

Where h again, is the effective mixed layer depth (same as Equation 7) and $K_{z,eff}$ is the effective vertical diffusivity of the one-dimensional model. The one-dimensional model's $K_{z,eff}$ must match that of the ocean component of the ESM in order for the growth of C_{ant} uptake of the one-dimensional model to match that of the ocean component of the ESM (Gnanadesikan et al., 2015). Diagnosing an ocean model's mixed layer impulse response function diagnoses the net C_{ant} removal by simulated physical processes, and thus the $K_{z,eff}$ of the ocean model. However, diagnosing the mixed layer impulse response function requires special simulations (Joos et al., 1996), and is unnecessary if one instead uses h as tuning parameter (Meinshausen et al., 2011). Experiments with one-dimensional carbon cycle models show that $K_{z,eff}$ is indirectly tuned by adjusting h (Oeschger et al., 1975). Thus by changing h of the one-dimensional model, we can match the $K_{z,eff}$ of the CESM and therefore the one-dimensional model replicates CESM ocean C_{ant} uptake over the historical period.

https://doi.org/10.5194/bg-2020-254
Preprint. Discussion started: 16 July 2020

$C_{ant}(t)$ and F_{ant} are calculated explicitly by the one-dimensional model, and the second term on inside the integral in Equation 9, the diffusive C_{ant} flux, is not modeled explicitly by the one-dimensional model, but can be determined exactly by residual. In the one-dimensional model, the C_{ant} air-sea flux is calculated as follows:

$$F_{ant} = ck_g(pCO_2^{atm} - pCO_2^{ocn}) \tag{10}$$

F_{ant} is the ocean flux of anthropogenic carbon, which is dependent on the air-sea partial pressure gradient and the gas exchange coefficient (m^{-2} yr^{-1}). A conversion factor, c, converts the flux units from ppm m^{-2} yr^{-1} to mmol m^{-2} yr^{-1}. We calculate pCO_2^{ocn} as the preindustrial pCO_2^{ocn} ($pCO_2^{ocn,PI}$) plus an anthropogenic perturbation (δpCO_2^{ocn}). Model calculation of δpCO_2^{ocn} is based on a parameterization that includes effects of changing buffer capacity and temperature (Appendix B).

2.4 Process Decomposition Using One-Dimensional Ocean Carbon Cycle Model Simulations

Table 1. Description of the two experiments conducted with the one-dimensional carbon cycle model (Control and Constant Chemical Capacity), the historical scaling experiment, and the effects quantified from these experiments.

Experiment Name	Description	Symbol	Scenarios
All Effects (Control)	full chemistry	ΔC_{total}	RCP8.5, RCP4.5, 1.5°C
Constant Chemical Capacity	constant buffer factor	ΔC_{ccc}	RCP8.5, RCP4.5, 1.5°C
Historical Scaling[1]	constant efficiency	$\Delta \overset{*}{C}_{hs}$	RCP8.5, RCP4.5, 1.5°C
Effect Name	**Effect Symbol**		**Equation**
Carbon Gradient Effect	ΔC_{cgrad}		$\Delta C_{ccc} - \Delta \overset{*}{C}_{hs}$
Chemical Capacity Effect	ΔC_{chem}		$\Delta C_{total} - \Delta C_{ccc}$

1. $\Delta \overset{*}{C}_{hs}$ is calculated directly from pCO_2^{atm} ($\Delta \overset{*}{C}_{hs} = \int \overset{*}{F}_{ant}\, dt$; Equation 4)

We analyze two additional idealized one-dimensional model experiments for each scenario, for a total of 6 complementary simulations that are used to diagnose the changes seen in the CESM simulations. The naming convention for these experiments and a brief description are listed in Table 1. Cumulative change is denoted as ΔC_X. In addition to these simulations, we calculate cumulative C_{ant} uptake consistent with the historical scaling, $\Delta \overset{*}{C}_{hs}$, for each scenario. $\Delta \overset{*}{C}_{hs}$ is calculated directly from the prescribed pCO_2^{atm} (Table 1; Equation 4). With these experiments, we quantify how two negative effects, ΔC_{chem} and ΔC_{cgrad}, combine to make ΔC_{total} lower than the historical scaling ($\Delta \overset{*}{C}_{hs}$):

$$\Delta C_{total} = \Delta \overset{*}{C}_{hs} + \Delta C_{chem} + \Delta C_{cgrad} \tag{11}$$

Changes in ocean chemical capacity, ΔC_{chem}, are the change in C_{ant} in a one-dimensional model simulation with all effects, ΔC_{total} , minus the change in C_{ant} in a one-dimensional model simulation with constant chemical capacity, ΔC_{ccc} (Table 1). The carbon gradient effect, ΔC_{cgrad}, is the difference between ΔC_{ccc} and the time integral of $\overset{*}{F}_{ant}$, $\Delta \overset{*}{C}_{hs}$. The carbon

https://doi.org/10.5194/bg-2020-254
Preprint. Discussion started: 16 July 2020

Biogeosciences Discussions Open Access EGU

gradient effect is due to interactions between the transport of C_{ant} out of the surface ocean and the growth rate of pCO_2^{atm}. Because circulation is fixed in the one-dimensional ocean carbon cycle model, changes to the carbon gradient effect are not due to changes in circulation. In the results, we show that ocean C_{ant} uptake has a low sensitivity to simulated changes in circulation from 1920-2080.

2.5 C_{ant} Air-Sea Flux Decomposition

We use the one-dimensional model to identify the dominant controls on ocean C_{ant} uptake, by decomposing the C_{ant} air-sea flux into multiple terms. In order to perform this decomposition, surface ocean pCO_2^{ocn} must be represented by a single value (Equation 10). For the ocean component of the ESM, defining an effective pCO_2^{ocn}, representing the entire surface ocean, is not straightforward due to the spatial variability of pCO_2^{ocn}. Therefore, this decomposition is only feasible in the one-dimensional ocean carbon cycle model.

The C_{ant} air-sea flux can be considered to be a function of three indirectly related variables: $F_{ant}(pCO_2^{atm}, C_{ant}, T)$. Because these variables are indirectly related, we can decompose the total derivative of the C_{ant} air-sea flux ($\frac{dF_{ant}}{dt}$) into its partial derivatives:

$$\frac{dF_{ant}}{dt} = \underbrace{\overbrace{\frac{\partial pCO_2^{atm}}{\partial t}}^{atm.\ gr.\ rate} \frac{\partial F_{ant}}{\partial pCO_2^{atm}}}_{atmos.\ component} + \underbrace{\overbrace{\frac{\partial pCO_2^{ocn}}{\partial t}}^{ocn.\ gr.\ rate} \frac{\partial F_{ant}}{\partial pCO_2^{ocn}}}_{ocean\ component} \tag{12}$$

The first term on the right hand side is the impact of the atmospheric CO_2 growth rate on the flux (atmosphere component) and the second term is the impact of the ocean CO_2 growth rate on the flux (ocean component). In Equation 12, $\frac{\partial F_{ant}}{\partial pCO_2^{atm}} = \frac{\partial F_{ant}}{\partial pCO_2^{ocn}}$, and is constant, thus variations in F_{ant} are solely due to variations in the atmospheric CO_2 growth rate and the ocean CO_2 growth rate. The pCO_2^{ocn} closely follows pCO_2^{atm}, and the sign of their growth rates is the same. When the atmospheric CO_2 growth rate is positive, the atmospheric CO_2 growth rate acts to enhance F_{ant}, and the ocean CO_2 growth rate acts to decrease F_{ant} (Equation 10). The atmospheric CO_2 growth rate is prescribed, and cannot be separated further in this framework, while the ocean component is expanded into the following terms:

$$\frac{\partial pCO_2^{ocn}}{\partial t} = \frac{\partial C_{ant}}{\partial t} \frac{\partial pCO_2^{ocn}}{\partial C_{ant}} + \frac{\partial T}{\partial t} \frac{\partial pCO_2^{ocn}}{\partial T} \tag{13}$$

The two ocean terms are the product of the change in C_{ant} times the buffer factor, and the change in temperature times the sensitivity of pCO_2^{ocn} to warming. Substituting Equation 8 we arrive at three terms controlling the ocean component:

$$\frac{\partial pCO_2^{ocn}}{\partial t} = \underbrace{\frac{F_{ant}}{h} \overbrace{\frac{\partial pCO_2^{ocn}}{\partial C_{ant}}}^{buffer\ factor}}_{impact\ of\ air-sea\ flux} + \underbrace{\frac{K_{z,eff}}{h} \frac{\partial C_{ant}}{\partial z} \overbrace{\frac{\partial pCO_2^{ocn}}{\partial C_{ant}}}^{buffer\ factor}}_{impact\ of\ ocean\ circ.} + \underbrace{\frac{\partial T}{\partial t} \overbrace{\frac{\partial pCO_2^{ocn}}{\partial T}}^{warm.\ sens.}}_{impact\ of\ warming} \tag{14}$$

https://doi.org/10.5194/bg-2020-254
Preprint. Discussion started: 16 July 2020


Biogeosciences Discussions

We refer to the three terms on the right hand side, from left to right, as the impact of the air-sea flux on pCO_2^{ocn}, the impact of ocean circulation on pCO_2^{ocn}, and the impact of warming on pCO_2^{ocn}. Because the impact of warming is small, the ocean CO_2 growth rate is a balance between the impact of the air-sea flux on pCO_2^{ocn} and the impact of ocean circulation on pCO_2^{ocn}. The sign of F_{ant} is always positive in all scenarios, thus the impact of the air-sea flux always acts to increase pCO_2^{ocn}. The sign of the vertical gradient ($\frac{\partial C_{ant}}{\partial z}$) is always negative, thus the impact of ocean circulation always acts to decrease pCO_2^{ocn}. In the ΔC_{total} experiment (Table 1), F_{ant}, the vertical C_{ant} gradient, the buffer factor, and sensitivity to warming, are freely evolving (Equation 14). In the ΔC_{ccc} experiment, the buffer factor is fixed at preindustrial values. The $\Delta \overset{*}{C}_{hs}$ experiment is equivalent to a constant buffer factor, a warming sensitivity of 0, and, as shown in the results, setting the C_{ant} profile to that predicted by historical scaling. The vertical profile alters pCO_2^{ocn} through the vertical gradient (Equation 14). In the results we will use Equation 14 to illustrate how changes to the impact of ocean circulation result in reduced efficiency of ocean C_{ant} uptake in response to emission mitigation.

3 Results

In the following sections, we use ocean output from the ocean component of the ESM to calculate the efficiency of ocean C_{ant} uptake (Results 3.1) and determine if the evolution of C_{ant} concentration along meridional sections is consistent with historical scaling (Results 3.2). We then use the one-dimensional model to attribute changes in the efficiency of C_{ant} uptake to physical and/or chemical mechanisms (Results 3.3). Changes to the air-sea flux arising from changes to the atmospheric CO_2 growth rate and ocean CO_2 growth rate are also diagnosed (Results 3.4). Our analysis includes scenarios with aggressive emission mitigation (1.5°C), intermediate emission mitigation (RCP4.5), and no emission mitigation (RCP8.5). See Figure 2c for the pCO_2^{atm} forcing for these scenarios.

3.1 Projected Spatial Redistribution of the C_{ant} Air-Sea Flux

Using output from the ocean component of the ESM, we diagnose C_{ant} air-sea flux for three future scenarios: 1.5°C, RCP4.5, RCP8.5. Here we focus on the projected spatial distribution of C_{ant} air-sea flux from 2020-2080.

In the 1.5°C scenario the spatial pattern of the C_{ant} air-sea flux changes significantly from 2020-2080. While most of the ocean is a sink in 2020, in 2050 and 2080 there are large regions of C_{ant} outgassing (Figure 1, bottom row). Most pronounced is the emergence of C_{ant} outgassing in the equatorial Pacific. The outcrop region of Sub-Antarctic Mode Water (SAMW) at about 50°S also experiences outgassing by 2080. In 2020, the Kuroshio and subpolar North Atlantic are some of the most intense sinks of C_{ant}, but by 2080, these regions are sources. The Equatorial Pacific, SAMW outcrop region, Kuroshio, and subpolar North Atlantic are broad regions that are sources of C_{ant} in 2080 under the 1.5°C scenario. Contrastingly, Southern Ocean C_{ant} uptake persists throughout the simulation.

In the RCP4.5 scenario, changes to the spatial pattern lie somewhere between RCP8.5 and the 1.5°C scenario. Equatorial Pacific outgassing of C_{ant} grows over time, but is less widespread and intense than in the 1.5°C scenario (Figure 1, middle row). C_{ant} air-sea flux intensity decreases over time for the subpolar and mid-latitude Atlantic and Kuroshio region. Beyond

https://doi.org/10.5194/bg-2020-254
Preprint. Discussion started: 16 July 2020

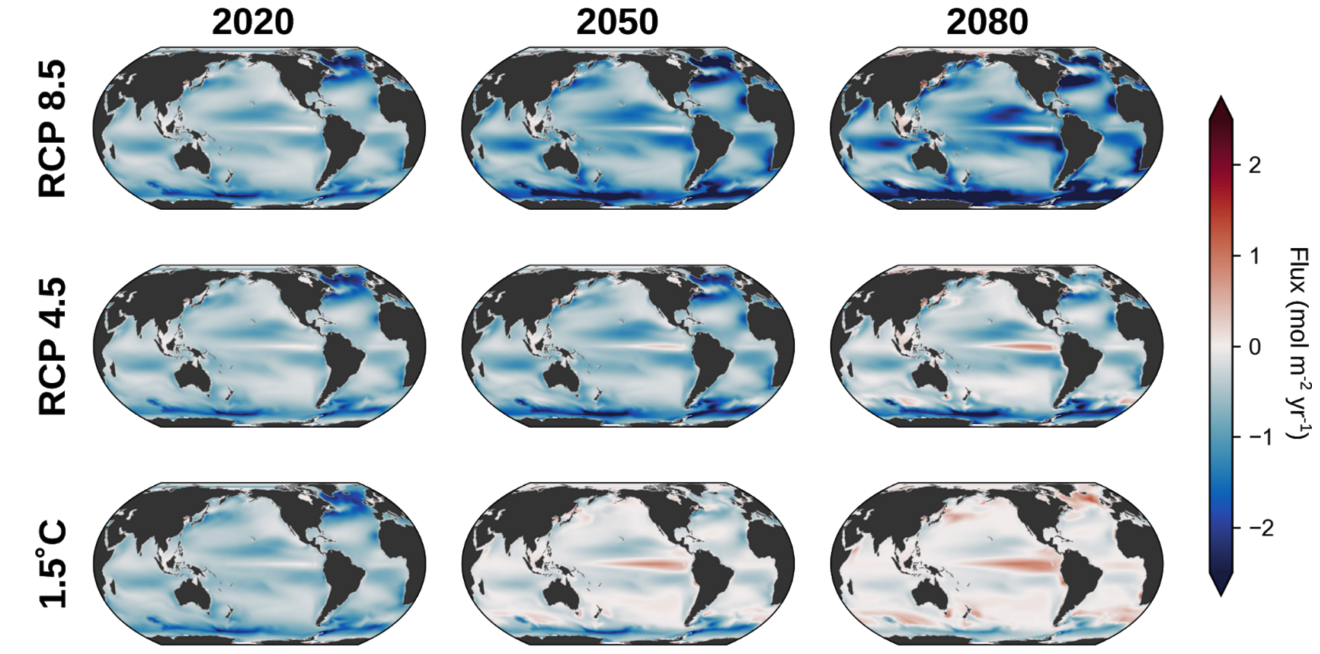

Figure 1. Ocean component of the ESM output of air-sea flux (mol C_{ant} m^{-2} yr^{-1}; positive = red = to the atmosphere). Ensemble mean is presented to reduce the potential effect of interannual variability masking the forced response. Negative indicates into the ocean. Each row is a scenario, and each column represents a year. Emission mitigation is greatest at the bottom of each column.

the equatorial Pacific, the spatial pattern of C_{ant} air-sea flux is similar to the RCP8.5 scenario, but the amplitude of uptake is reduced.

Relative to the scenarios with emission mitigation (1.5°C and RCP4.5) the RCP8.5 scenario features a consistent spatial pattern of the C_{ant} air-sea flux (Figure 1, top row). The primary change over time is an amplification of magnitude, with the highest flux intensity occurring in 2080.

Ocean C_{ant} uptake is greatest in RCP8.5, and is the lowest in 1.5°C (Figure 2a). In all scenarios ocean C_{ant} inventory increases throughout the period (Figure 2d). In the RCP4.5 scenario, C_{ant} air sea flux peaks in 2050, and then gradually declines. In the 1.5°C scenario, ocean C_{ant} uptake peaks in 2020, and is almost zero by 2080. In the RCP4.5 scenario ocean C_{ant} uptake initially increases and then returns to 2020 values by 2080.

Extrapolation of the ocean C_{ant} uptake based on the historical scaling ($\overset{*}{F}_{ant}$) is dependent solely on pCO_2^{atm}. Lower pCO_2^{atm} results in a lower estimate of ocean C_{ant} uptake, and higher pCO_2^{atm} results in greater uptake. In all scenarios, simulated air-sea C_{ant} uptake is far less than $\overset{*}{F}_{ant}$ (Figure 2a). Reduced uptake relative to $\overset{*}{F}_{ant}$ indicates that in the future, ocean C_{ant} uptake will be less efficient (Figure 2b). Efficiency is the ratio of the solid lines (F_{ant}) to the respective dashed lines ($\overset{*}{F}_{ant}$) in Figure 2a, with this ratio plotted in Figure 2b. Efficiency (Figure 2b) remains greater than 90% from 1990 through 2010, but then declines under all future scenarios, with greater efficiency declines as emission mitigation increases.

https://doi.org/10.5194/bg-2020-254
Preprint. Discussion started: 16 July 2020

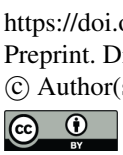

Biogeosciences Discussions Open Access EGU

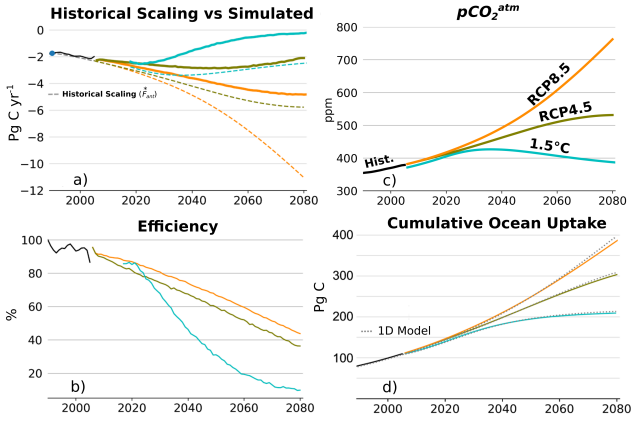

Figure 2. (a) Historical scaling of ocean C_{ant} uptake ($\overset{*}{F}_{ant}$; dotted lines) and simulated (ocean component of the ESM) ocean C_{ant} uptake (F_{ant}; solid lines) for three scenarios (1.5°C, RCP4.5, and RCP8.5). Negative indicates atmospheric C_{ant} removal. (b) Simulated (ocean component of the ESM) efficiency for the three scenarios. (c) Atmospheric CO_2concentration. (d) Simulated ocean C_{ant} accumulation (solid lines) and the one-dimensional model C_{ant} accumulation (dotted lines). Air-sea flux and efficiency from 2006-2017 not shown for 1.5°C scenario due to ocean adjustment to pCO_2^{atm} forcing (see Methods 2.2; Figure S2).

The efficiency decrease is linear in RCP8.5 and RCP4.5, but exponential in the 1.5°C scenario. The 1.5°C scenario is the only scenario with negative pCO_2^{atm} growth rates, which substantially modifies the ocean carbon cycle response, as shown below.

3.2 Projected Changes in the Ocean Interior

Here we analyze the evolution of the C_{ant} vertical gradient by applying the historical scaling to the vertical profile of C_{ant} (Equation 6). A weakening of the vertical gradient of C_{ant} would reduce the ability of physical removal of C_{ant} to maintain the C_{ant} air-sea flux (F_{ant}; Equation 14). Thus, via the vertical C_{ant} gradient, interior C_{ant} can alter the air-sea flux. Deviations of globally averaged C_{ant} profiles ($C_{ant}(z)$) from the C_{ant} historical scaling ($\overset{*}{C}_{ant}(z)$) are defined as $C_{ant}(z) - \overset{*}{C}_{ant}(z)$. Wherever $C_{ant}(z) > \overset{*}{C}_{ant}(z)$, more carbon is stored at that location than predicted by the C_{ant} historical scaling (Equation 6) and the deviation is positive. Assuming ocean circulation remains constant, if deviations are less at the surface relative to the interior, the vertical gradient would be weaker than expected by the historical scaling, and thus ocean C_{ant} uptake would be less efficient. Therefore the historical scaling may be used to identify how the pattern of changing interior $C_{ant}(z)$ deviates from the historical scaling (Figure 3) and thus reduces the efficiency of the C_{ant} air-sea flux (Figure 2b). With more rapid emission mitigation, globally average profiles reveal a pattern of increasingly positive deviations from the historical scaling at depth (Figure 3).

In the RCP8.5 and RCP4.5 scenarios, $C_{ant}(z)$ increases from 2020-2080 at all depths, but at the surface, $C_{ant}(z)$ increase is less than $\overset{*}{C}_{ant}(z)$ increase (Figure 3a). In the RCP4.5 scenario, the C_{ant} at depth is greater than $\overset{*}{C}_{ant}(z)$, while in the RCP8.5 scenario it is less than $\overset{*}{C}_{ant}(z)$ (Figure 3b). In both the RCP8.5 and RCP4.5 scenarios, the increase in C_{ant} is surface

https://doi.org/10.5194/bg-2020-254
Preprint. Discussion started: 16 July 2020

intensified, which enhances the vertical gradient. The enhanced vertical gradient allows for increased vertical diffusion of C_{ant}, and thus increased ocean C_{ant} uptake. However, in RCP4.5 and RCP8.5 the enhancement of the vertical gradient is not as strong as the historical scaling would suggest (Figure 3b). In the 1.5°C scenario, the largest change in $C_{ant}(z)$ is at depth, and at the surface C_{ant} decreases. This results in a much weaker vertical gradient, weaker vertical diffusion, and thus a reduced ocean C_{ant} uptake. The surface loss of C_{ant} is a short term response to declines in pCO_2^{atm} that began in 2036, while the increase in $C_{ant}(z)$ at depth is from the long-term increase in pCO_2^{atm} relative to preindustrial times (Figure 3c).

The signals found in $C_{ant}(z)$ are found throughout the ocean (Figure 4). In the RCP8.5 scenario (Figure 4, top row), the surface layer exhibits the strongest negative deviation, but there is no positive deviation in the interior. The negative deviation is seen in deep waters between 25°N and 60°N, and also in the bowls of the northern and southern subtropical gyres. The negative deviation grows from 2020-2080, and appears to propagate into the ocean interior with NADW. The historical scaling alone cannot identify whether buffering or solubility is the driver of lower $C_{ant}(z)$ than $\overset{*}{C}_{ant}(z)$ in the interior.

In the RCP4.5 scenario, the surface layer exhibits a growing negative deviation (Figure 4, middle). The negative surface deviation spans from the southern to the northern end of the zonal mean section. In the interior, however, there is a growing positive deviation. The magnitude and growth rate of the interior positive deviation is less than in the 1.5°C scenario. The positive deviation is due to the lagged response of the ocean interior to the intermediate rate of emission mitigation in RCP4.5, in which pCO_2^{atm} slowly plateaus (Figure 2c).

The 1.5°C scenario features the largest positive C_{ant} deviations from the historical scaling (Figure 4, bottom row). The positive deviation is found throughout the thermocline. These are waters that outcrop in the equatorial Pacific and mid to high latitudes, consistent with these regions being a source of C_{ant} by 2080 (Figure 1). In the next section, we will evaluate the relative role of buffering for all scenarios.

3.3 Drivers of Simulated Changes in Efficiency

We utilize projections of ocean C_{ant} uptake from the one-dimensional model to provide mechanistic understanding of the changes in ocean carbon uptake efficiency simulated by the full model. Changes in ocean C_{ant} are examined to determine what drives projected changes in efficiency. These changes that are quantified with the one-dimensional model are separated into the carbon gradient effect, ΔC_{cgrad} (Table 1), and effects related to the ocean's chemical capacity to absorb carbon, ΔC_{chem} (Table 1). The one-dimensional model can accurately recreate the change in C_{ant} inventory for all scenarios (Figure 2d), indicating that the assumption of constant circulation and parameterized chemistry are reasonable through 2080. For the RCP8.5 scenario, the difference between the one-dimensional model cumulative flux and ocean component model is the largest. The cumulative error is 4 Pg C_{ant}, only 3% of the 2080 cumulative flux, again indicating that the one-dimensional model is a useful diagnostic tool for quantifying changes in the efficiency of ocean uptake .

Over the historical forcing period (1920-2006) ΔC_{cgrad} drives ΔC_{total} to be slightly lower than the historical scaling (Figure 5). Because there is no internal ocean variability in the one-dimensional model (constant ocean circulation), ΔC_{cgrad} in this period is due to only the integrated effects of short term variations in the growth rate of the pCO_2^{atm} forcing, which drive a slight reduction in total uptake (McKinley et al., 2020).

https://doi.org/10.5194/bg-2020-254
Preprint. Discussion started: 16 July 2020

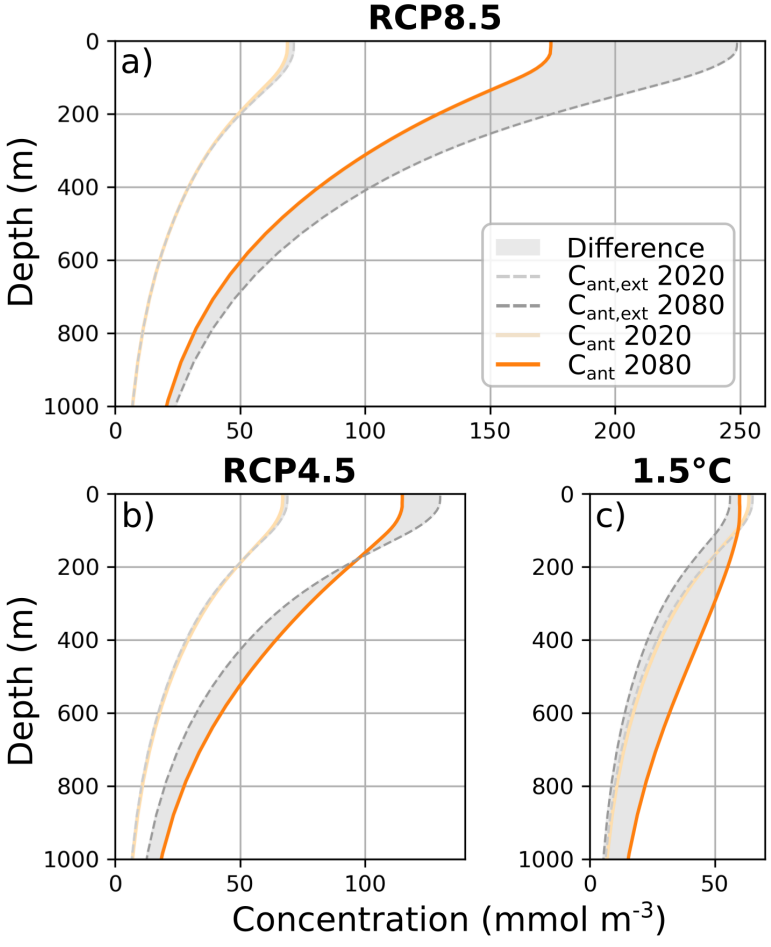

Figure 3. Output from the ocean component of the CESM of the global mean C_{ant} profiles ($C_{ant}(z)$) (orange, solid), and profiles of $\overset{*}{C}_{ant}(z)$ (gray, dashed), for the (a) RCP8.5 scenario, (b) RCP4.5 scenario, and (c) 1.5°C scenario. The shaded region between the dashed and solid lines indicates the deviation from the historical scaling. Light lines are for 2020 and dark lines are for 2080. The shaded region between the lines is shown for zonal mean sections in Figure 4.

https://doi.org/10.5194/bg-2020-254
Preprint. Discussion started: 16 July 2020

Biogeosciences Discussions Open Access EGU

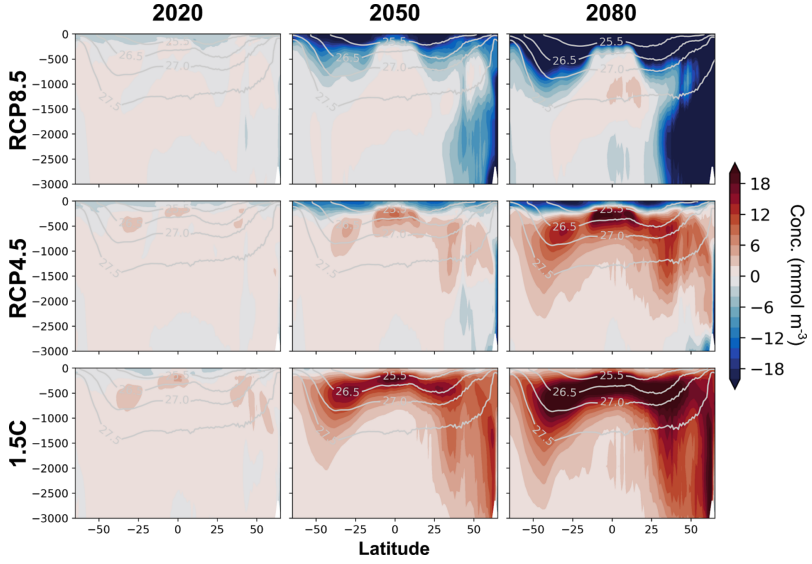

Figure 4. Ocean component model output of the global zonal mean deviation of C_{ant} concentration (mmol m^{-3}) from the historical scaling of C_{ant} ($C_{ant} - \overset{*}{C}_{ant}$). Rows and columns same as Figure 1. Positive regions indicate faster carbon accumulation than historical scaling, negative regions indicate slower accumulation. Contour lines are surfaces (kg m^{-3}).

In RCP8.5, the ocean cumulatively absorbs 393 Pg C_{ant} (Figure 5) by 2080, approximately 2.5 times the present-day C_{ant} inventory (160-166 Pg C_{ant}; Devries, 2014). In RCP8.5, the historical scaling tracks the simulation with constant chemical capacity (Figure 5). This indicates that if ocean chemical capacity remains constant, the ocean would absorb an additional 158 Pg C_{ant}. The positive ΔC_{cgrad} is attributable to fitting CESM C_{ant} uptake to a not-quite exponential pCO_2^{atm} in the historical period. Changes in ocean C_{ant} uptake due to warming were calculated, but are not shown as warming effects are small relative to ΔC_{chem}, making up <5% of the total efficiency decline. This small contribution is consistent with the change due to warming calculated in studies of climate-carbon feedbacks (Randerson et al., 2015, Schwinger et al., 2018).

In RCP4.5, the ocean absorbs 307 Pg C_{ant} (Figure 5) by 2080. Cumulative uptake predicted by the historical scaling tracks the constant chemical capacity simulation until around 2040 (Figure 5). After 2040, the historical scaling and the constant chemical capacity simulation diverge, indicating the increasing carbon gradient effect is related to the decreasing growth rate of the pCO_2^{atm} forcing in this time frame. The ΔC_{cgrad} effect amounts to -52 Pg C_{ant} in 2080, however, the ΔC_{chem} effect is stronger, amounting to -84 Pg C_{ant} by 2080.

In the 1.5°C scenario, the ocean absorbs 213 Pg C_{ant} (Figure 5) by 2080. The ΔC_{chem} effect is the weakest in this scenario, -37 Pg C in 2080. The weak ΔC_{chem} effect is consistent with this scenario taking up the least C_{ant} because chemical capacity decreases as C_{ant} uptake increases. ΔC_{cgrad} is the dominant change in this scenario, accounting for -90 Pg C_{ant}. The strongly reduced vertical gradient of C_{ant} (Figure 3,4) results in reduced vertical C_{ant} removal (Equation 8).

https://doi.org/10.5194/bg-2020-254
Preprint. Discussion started: 16 July 2020

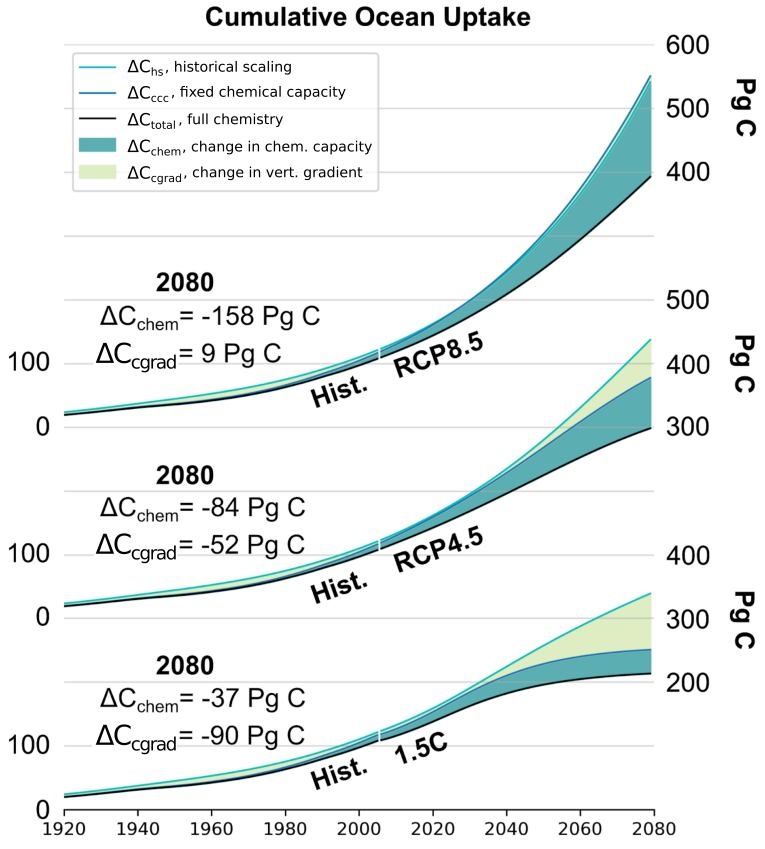

Figure 5. Cumulative ocean C_{ant} uptake (Pg C) for the historical period and the three scenarios in the one-dimensional model. The cyan line is the extrapolation based on the historical scaling. The dark blue line is the one-dimensional model simulation of constant chemical capacity (PI buffer factor) with variable solubility. The black line is the one-dimensional model simulation that includes all effects (variable chemical capacity and variable solubility). Light green shading represents decreases in uptake related to the carbon gradient effect (ΔC_{cgrad}), teal shading represents decreases in uptake related to chemical capacity (ΔC_{chem}). Negative indicates loss of ocean carbon.

3.4 Decomposition of the C_{ant} Air-Sea Flux

Here we diagnose the mechanisms controlling the C_{ant} air-sea flux (F_{ant}) in the one-dimensional model ΔC_{total} simulations. The one-dimensional model has been tuned so the ΔC_{total} simulation matches the CESM (Figure 2d). The one-dimensional form of the model allows for the decomposition of C_{ant} air-sea flux (Methods 2.5).

Air-sea flux (F_{ant}) in the one-dimensional model is controlled by large opposing components (Figure 6), the atmosphere component, driven by the atmosphere CO_2 growth rate, and the ocean component, driven by the ocean CO_2 growth rate. Because the air-sea flux is adding C_{ant} to the surface in all simulations, the impact of the air-sea flux on pCO_2^{ocn} is to increase pCO_2^{ocn}, while the impact of ocean circulation is to decrease pCO_2^{ocn} because of the downward vertical C_{ant} gradient

https://doi.org/10.5194/bg-2020-254
Preprint. Discussion started: 16 July 2020

Biogeosciences Discussions Open Access EGU

(Equation 14). Thus the vertical C_{ant} gradient plays an important role in sustaining C_{ant} removal by ocean circulation, and thus slowing the ocean CO_2 growth rate.

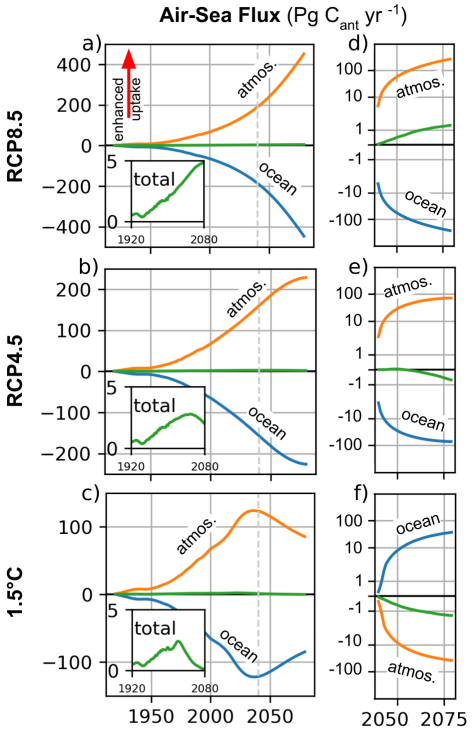

Figure 6. (a-c) Total C_{ant} air-sea flux (green line; Pg C_{ant} yr^{-1}) and its ocean (blue line; Pg C_{ant} yr^{-1}) and atmosphere (orange line; Pg C_{ant} yr^{-1}) components. The values for the air-sea flux and its components are calculated by integrating the C_{ant} air-sea flux growth rate ($\frac{dF_{ant}}{dt}$, units of Pg C_{ant} yr^{-2}), and the ocean component ($\frac{\partial pCO_2^{ocn}}{\partial t}\frac{\partial F_{ant}}{\partial pCO_2^{ocn}}$, units of Pg C_{ant} yr^{-2}) and atmosphere component ($\frac{\partial pCO_2^{atm}}{\partial t}\frac{\partial F_{ant}}{\partial pCO_2^{atm}}$, units of Pg C_{ant} yr^{-2}), from left to right, starting at the beginning of the simulation in 1850. The annual air-sea flux is shown on a reduced axis in (a-c). In (d-f) the same terms (Equation 12) are integrated starting in 2040 (vertical dashed line in (a-c)) and on a log scale to highlight the changing roles of the ocean and atmosphere components under rapid mitigation scenarios. Components are non-zero at 2040 in (d-f) because of the air-sea pCO_2 difference in 2040.

In the RCP8.5 scenario, the atmosphere component acts to enhance F_{ant}, and the ocean component acts to reduce the F_{ant} (Figure 6a-b). The actual F_{ant} (Figure 6, green) is a small residual of these tendencies. Increasing pCO_2^{atm} acts to increase
385 the air-sea pCO_2 difference, while increasing pCO_2^{ocn} acts to decrease F_{ant} (Equation 12). If pCO_2^{ocn}, increased only very slightly, such as the hypothetical scenario where the ocean is well mixed from surface to deep, ocean C_{ant} uptake would be the magnitude of the atmospheric component (Figure 6a-b). In fact, the ocean component is also subject to a balance between two large terms. The increase in pCO_2^{ocn} is mitigated by ocean circulation, thus ocean circulation enhances F_{ant} (Equation 14). F_{ant} increases pCO_2^{ocn} and, which in turn reduces F_{ant} (Equation 14).

https://doi.org/10.5194/bg-2020-254
Preprint. Discussion started: 16 July 2020

In the RCP4.5 scenario, the atmosphere and ocean components acts similarly to the RCP8.5 scenario, with the atmosphere component enhancing F_{ant}, while the ocean component acts to reduce F_{ant} (Figure 6c-d). However, due to increased emission mitigation, pCO_2^{atm} plateaus (Figure 2c), and in 2040 F_{ant} begins to decline. The ocean component is acting to decrease F_{ant} and by 2040 overwhelms the atmosphere component. The pCO_2^{ocn} increases slower than pCO_2^{atm}, which acts to enhance the flux early in the period, but the slower rate of change of pCO_2^{ocn} cause F_{ant} to decline in the later period (Figure 6d).

In the 1.5°C scenario, initially the atmosphere component acts to enhance F_{ant}, and the ocean component acts to reduce F_{ant}. However, by 2040, the roles of F_{ant} components have switched (Figure 6a-b). Due to rapid emission mitigation, pCO_2^{atm} plateaus, and then begins to decrease slightly, acting to reduce F_{ant} for the first time since the preindustrial era. After 2040, the ocean component acts to enhance F_{ant} (Figure 6f). If efficiency were constant, it follows that the ratio of atmosphere to ocean components is constant and the change in pCO_2^{ocn} for a a given change in pCO_2^{atm} ($\frac{\Delta pCO_2^{ocn}}{\Delta pCO_2^{atm}}$) would also be constant. From 2013 to 2036, the year of pCO_2^{atm} begins to decline (Figure 2c), pCO_2^{atm} increases 39 ppm, and pCO_2^{ocn} increases 39 ppm and $\frac{\Delta pCO_2^{ocn}}{\Delta pCO_2^{atm}} = 1.00$. From 2036 to 2080, pCO_2^{atm} also declines 39 ppm and pCO_2^{ocn} declines 37 ppm, thus $\frac{\Delta pCO_2^{ocn}}{\Delta pCO_2^{atm}} = 0.95$. From 2040 to 2080, the $C_{ant}(z)$ has weakened relative to the historical scaling (Figure 4), thus also weakening the impact of ocean circulation on pCO_2^{ocn} (Equation 14). The weakening of the vertical C_{ant} gradient therefore plays a significant role in reducing $\frac{\Delta pCO_2^{ocn}}{\Delta pCO_2^{atm}}$, and thus efficiency, on the downward pCO_2^{atm} trajectory.

4 Discussion

4.1 Drivers of Future Efficiency Declines

Ocean carbon uptake will decline as a result of emission mitigation. We also show that the efficiency of ocean carbon uptake, i.e. how closely ocean carbon uptake follows the observed proportionality between uptake and atmospheric CO_2, is also reduced as mitigation becomes more rapid, consistent with the results of Raupach et al. (2014). Under exponentially increasing pCO_2^{atm} (RCP8.5), reductions in efficiency of ocean C_{ant} uptake are almost entirely due to reduced buffer capacity. We find that an exponentially increasing pCO_2^{atm} allows for the entire vertical C_{ant} profile to behave as a function of pCO_2^{atm}. Because ocean C_{ant} uptake is well characterized by one-dimensional physics, under constant chemistry and ocean circulation, if the vertical profile behaves as a function of pCO_2^{atm} then air-sea flux will also behave as function of pCO_2^{atm} (Equation 4, Equation 8). With rapid mitigation, the vertical C_{ant} profile, which is set by the integrated effects of past C_{ant} accumulation at depth, does not change to immediately to adjust to the trajectory of pCO_2^{atm}. We find that in a scenario featuring rapid emission mitigation (1.5°C), the C_{ant} concentration change from 2020-2080 is greatest in the thermocline, a behavior that has been identified in other simulations of rapid emission mitigation (Tokarska et al., 2019). The past C_{ant} accumulation at depth weakens the vertical C_{ant} gradient compared to a vertical C_{ant} profile that reaching the same pCO_2^{atm} under exponential pCO_2^{atm} increase, constant ocean chemistry, and constant circulation (Figure 3).

The air-sea flux is a balance between the atmospheric CO_2 growth rate and the ocean CO_2 growth rate (Equation 12), and in all scenarios the atmospheric CO_2 growth rate dominates the balance. The positive atmospheric CO_2 growth rates throughout the RCP8.5 and RCP4.5 scenarios acts to enhance the air-sea flux. In the 1.5°C scenario, ocean pCO_2^{atm} declines after 2036,

https://doi.org/10.5194/bg-2020-254
Preprint. Discussion started: 16 July 2020


Biogeosciences Discussions Open Access EGU

and the negative atmospheric CO_2 growth rate acts to decrease the air-sea flux, while the negative ocean CO_2 growth rate acts to enhance the air-sea flux. The negative growth rates of the 1.5°C scenario occur in the only scenario where efficiency declines exponentially.

The dominant mechanisms governing the decline in efficiency are different in each scenario, due to the differing degrees of emission mitigation. Internal ocean mechanisms (reduced chemical capacity) dominate the reduction of efficiency in the RCP8.5 scenario, and external mechanisms (increasing carbon gradient effect) dominate the reduction of efficiency in the 1.5°C scenario. For the ocean, warming effects have a small impact relative to the carbon gradient and chemical capacity effects.

The growing carbon gradient effect in the 1.5°C scenario is due to a weakening of the C_{ant} vertical gradient, thus a declining rate at which C_{ant} mixes and diffuses into the ocean interior. The magnitude of the C_{ant} air-sea flux is limited by the rate of surface C_{ant} removal (Graven et al., 2012), thus slower removal results in a reduced growth rate of ocean C_{ant} uptake. The vertical gradient is weaker in scenarios with slower than exponential pCO_2^{atm} increase, compared to the vertical gradient at the same pCO_2^{atm} concentration in an exponentially increasing pCO_2^{atm} scenario, because C_{ant} concentration is enhanced at depth relative to exponential scenarios (Figure 3,4). The C_{ant} concentration is elevated at depth because it takes longer for the slower than exponential scenarios to reach the same pCO_2^{atm}, allowing more cumulative C_{ant} transfer to deeper waters. The waters at depth effectively push back on the changes occurring at the surface due to changing pCO_2^{atm}, which is qualitatively similar to how back-pressure in a pipe slows the flow of fluid through the pipe. It is the C_{ant} at depth that is providing the "back-pressure", resisting the flow of C_{ant} into the interior. The faster emissions are mitigated, the more evident the back-pressure exerted by ocean interior C_{ant} becomes (Figure 3,4,5,6). However, delaying emission mitigation would act to increase the total back-pressure effect that would eventually occur. If the RCP8.5 scenario is followed into the 22nd century, future emissions would be flat from 2100 to 2150 and then decline dramatically (van Vuuren et al., 2011). As pCO_2^{atm} growth slows in response to the declining rate of emissions, the back-pressure effect from the ocean will appear, but at a greater magnitude due to the much greater load of C_{ant} in the interior ocean. Therefore, climate simulations extending beyond 2100 are needed to quantify the back-pressure effect in high emission scenarios.

With aggressive emission mitigation, regional patterns of the C_{ant} air-sea flux shift, with implications for regional carbon cycle monitoring (Peters et al., 2017). The surface waters of regions that trend towards C_{ant} outgassing under emission mitigation (Figure 1; bottom row) are renewed by advection with waters that are much older than the waters that renew the waters of the subtropics (Toyama et al., 2017). As emissions are mitigated from 2020-2080, there is a positive change in C_{ant} concentration in the ocean interior, with this back-pressure effect being most pronounced at ∼400m (Figure 3). Regionally, advective fluxes are important drivers of C_{ant} reemergence (Bopp et al., 2015), thus the regional impacts of ocean circulation on pCO_2^{ocn} (Equation 14) would include the effects of advective fluxes in addition to mixing/diffusive fluxes (which dominate globally). In the outgassing regions of Figure 1 (bottom row), advective fluxes bring waters with an increasing load of C_{ant} to the surface, thus reemergence is increasing, acting to increase pCO_2^{ocn}. The increase in reemergence ultimately overwhelms the weakening downwards diffusive C_{ant} flux that acts to decrease pCO_2^{ocn}. Therefore, advection of C_{ant} is driving the C_{ant} air-sea flux further towards outgassing in the equatorial Pacific, supbolar and mid-latitude North Atlantic, SAMW outcrop region, and the

https://doi.org/10.5194/bg-2020-254
Preprint. Discussion started: 16 July 2020


Biogeosciences Discussions Open Access EGU

Kuroshio (Toyama et al., 2017). The Circumpolar Deep Water (CDW) that is upwelled into the surface of the Southern Ocean south of 50°S, is old relative to the subtropics, but it is uncontaminated by C_{ant}. Below ~400m the magnitude of the back-pressure decreases, therefore upwelling of CDW does not result in an increasing load of C_{ant} being brought to the surface. Southern Ocean C_{ant} uptake persists because the positive C_{ant} tendency is absent in the upwelling watermass.

The back-pressure from C_{ant} at depth is an unavoidable consequence of emission mitigation. While more efficient ocean C_{ant} uptake is desirable when drawing down pCO_2^{atm}, in fact, peak sink efficiency occurs under exponential growth of pCO_2^{atm}. How long the ocean will remain a net sink depends on the strength of the back-pressure effect, which depends on the strength of surface ocean C_{ant} removal. If the back-pressure effect is stronger, due to more vigorous ocean circulation transfer of C_{ant} to depth in the years prior to mitigation, the sink will disappear at a faster rate. With rapid mitigation, the ocean C_{ant} uptake peaks in approximately 2030 and nearly disappears by 2080. Despite the decline in the efficiency of ocean C_{ant} uptake under rapid mitigation, ESMs indicate that the ocean becomes the primary C_{ant} sink in scenarios with aggressive mitigation (Jones et al., 2013) and without mitigation (Randerson et al., 2015) because the land uptake declines more rapidly than ocean uptake (Zickfeld et al., 2016). The ocean will ultimately remove most atmospheric C_{ant} over tens of thousands of years (Archer, 2005, Archer et al., 2009).

4.2 Validity of the One-Dimensional Model Representation of Ocean Physics

Our one-dimensional ocean carbon cycle model represents multiple physical removal process as a single diffusive process (Equation 8). Parameterizing these various processes in this manner requires defining an effective vertical diffusivity of the ocean, $K_{z,eff}$ and better observational estimates of ocean mixing are required to in order to recreate the effective diffusivity of the actual ocean. In the three-dimensional ocean models used in ESMs, up to ~30% of simulated $K_{z,eff}$ is attributable to isopycnal eddy mixing (Gnanadesikan et al., 2015). Varying a three-dimensional ocean model's isopycnal eddy diffusivity within the range of typical model values results in a 92 Pg C range of cumulative ocean C_{ant} uptake under instantaneous CO_2 doubling (Gnanadesikan et al., 2015), thus the sensitivity of ocean C_{ant} uptake to isopycnal eddy mixing is much larger than the sensitivity to changing ocean circulation. Models with spatially varying isopycnal eddy diffusivities, such as the NCAR CESM and GFDL ESM2G, have parameterizations that produce a range of diffusivities from ~300 m^2s^{-1} in gyres, to ~1500 m^2s^{-1} in boundary currents (Dunne et al., 2012; Danabasoglu et al., 2011). Observational estimates of isopycnal eddy diffusivity from tracers (Ledwell et al., 1998) and satellite altimetry (Abernathey and Marshall, 2013) are uncertain, but consistently suggest that real world eddy diffusivities could be much higher, with ranges from ~1000 m^2s^{-1} in gyres, to ~10,000 m^2s^{-1} in boundary currents.

While the mean state of ocean circulation is most important over the never 60 years, as warming increases, the magnitude climate-carbon feedbacks increase, such as changes to ocean circulation driving changes in ocean carbon uptake (Randerson et al., 2015), which is not represented by our one-dimensional ocean carbon cycle model. The small effect of changing ocean circulation in our simulation is likely because changes due to declines in AMOC are not yet evident by 2080 (Sarmiento and LeQuéré, 1996; Randerson et al., 2015). While assuming that ocean climate-carbon feedbacks are small prior to 2080 is consistent with the behavior of the CESM (Randerson et al., 2015), this may not be hold true for the Earth System itself.

https://doi.org/10.5194/bg-2020-254
Preprint. Discussion started: 16 July 2020

The uncertainties associated with the timing and magnitude of climate-carbon feedbacks can be avoided by mitigating climate change (Randerson et al., 2015).

4.3 Identification of the Impacts of Internal Ocean Variability using the Historical Scaling

Given the direct relationship between the efficiency of ocean C_{ant} uptake and the deviations from the historical scaling, we suggest that future work quantify the impact of external mechanisms on observed interannual variability of ocean carbon uptake. The historical scaling relies on the assumption of fixed sink efficiency due to exponential growth of pCO_2^{atm}. While most of the industrial era is consistent with an exponential CO_2 growth, variability in emissions drives variability in the atmospheric growth rate that then results in decadal variability in the ocean carbon sink (McKinley et al., 2020). If the historical scaling is used to identify changes in observations of C_{ant} concentration (Gruber et al., 2019a), and the atmospheric growth rate has recently slowed, changes due to internal variability are mixed with signals related to the carbon gradient effect, and the changes due to internal variability (Gruber et al., 2019a) would be overestimated. We also emphasize that in a future with emission mitigation, deviations from historical scaling will not be driven by changes due to internal ocean variability alone, given the dynamic response of the ocean to changes in pCO_2^{atm}.

5 Conclusion

Atmospheric CO_2 has grown exponentially over the industrial era, and so has ocean C_{ant} concentration at all depths (DeVries, 2014; Gruber et al., 2019). Under the exponential forcing regime, ocean C_{ant} uptake also grows exponentially and, over the historical era, maintains high efficiency of ocean C_{ant} uptake as we have defined it here. In future scenarios, regardless of whether countries mitigate emissions, efficiency of ocean C_{ant} uptake will decline. However the mechanisms differ depending on the degree of mitigation. In the RCP8.5 scenario, a scenario with no emission mitigation, reduced buffer capacity explains nearly all of the loss in efficiency of ocean C_{ant} uptake by 2080, 158 Pg C. In the case of scenarios with emission mitigation, such as RCP4.5 and the 1.5°C scenario, the loss of efficiency is more due to the carbon gradient effect. The carbon gradient effect explains 38% of efficiency loss in RCP4.5 scenario, and 71% of the efficiency loss in the 1.5°C scenario. The carbon gradient effect increases with time in all scenarios with emission mitigation, and the equatorial Pacific becomes a prominent source of C_{ant} in both cases. Under aggressive mitigation (1.5°C) this carbon gradient effect will result in large regions of ocean becoming a source by 2080, with the exception of the Southern Ocean.

Changes in the vertical C_{ant} concentration gradient are responsible for this carbon gradient effect. Under exponential pCO_2^{atm} growth, with constant chemical capacity and constant solubility, the vertical C_{ant} gradient behaves as a function of pCO_2^{atm}, thus the C_{ant} air-sea flux behaves as though it is solely a function of pCO_2^{atm}, rather than a function of pCO_2^{atm}, C_{ant}, and temperature. When emissions are mitigated and the growth in pCO_2^{atm} slows, the surface ocean can respond rapidly. However, the ocean interior C_{ant} concentration response lags the surface response. Below 100m in the rapid mitigation scenario, C_{ant} concentration increases from 2020-2080, while above 100m, the C_{ant} concentration decreases, thus the downward C_{ant} concentration gradient is greatly reduced. A reduced downward vertical gradient results in less effective downward dif-

https://doi.org/10.5194/bg-2020-254
Preprint. Discussion started: 16 July 2020

fusion of C_{ant}. Ocean C_{ant} uptake is limited by surface ocean C_{ant} removal (Graven et al., 2012), thus this results in reduced uptake in the future, relative to ocean C_{ant} uptake under the same pCO_2^{atm} concentration in the historical period. This reduction of the vertical gradient, an unavoidable result of emission mitigation, is the driver of efficiency declines.

Under emission mitigation, the carbon gradient effect results in a enhanced outgassing of C_{ant} in the equatorial Pacific, and a transition from C_{ant} uptake to C_{ant} outgassing in the subpolar and mid-latitude North Atlantic, Kurshio, and SAMW outcrop region. These regions are also hotspots for reemergence (Bopp et al., 2015, Toyama et al., 2017). Reemergence of older watermasses, from depths where C_{ant} continues to increase, drives a tendency towards outgassing in these regions. The waters of the subtropics are renewed with shallower waters, above where the continued C_{ant} increase occurs in the ocean component of ESM, and the surface waters of the Southern Ocean are renewed with waters below the C_{ant} increase. Thus, in subtropics and Southern Ocean, the air-sea C_{ant} uptake continues.

Diffusive processes control the removal of C_{ant} from the surface ocean, and because the diffusivity of the surface ocean is highly uncertain, it creates large uncertainties in C_{ant} uptake (Gnanadesikan et al., 2015). Determining the effective vertical diffusivity of the upper ocean is essential to reducing uncertainty in future ocean C_{ant} uptake, particularly under 21st century emission mitigation scenarios.

Code and data availability. The code used to run the one-dimensional model is provided by the authors in a GitHub repository (https://qoccm.readthedocs.io/en/latest/). Raw output from the coupled ocean model simulations can download from NCAR's Earth System Grid (https://www.earthsystemgrid.org/).

Appendix A: Physical Interpretation of the Impulse Response Function Based Model one-dimensional model

Impulse response functions are a powerful tool in dynamical system analysis. With a response function, one can understand the response of a system to any pulse, as long as the response is linear. The response function used in our one-dimensional model has the same shape as the conceptual example in Figure A1. For the one-dimensional model case, the response function was derived by equilibrating HILDA to a doubling CO_2, and then tracking fraction of C_{ant} that remained in the surface box (the mixed layer) (Joos et al. 1996).

In our conceptual example of the mixed layer response function, at $t = 0$ 100% of the tracer remains in the mixed layer, while 200 years later, only 10% of the tracer remains (Figure A1). This is a general example of response function that can be applied to any transient tracer, but the values in this example have been scaled so that it is most similar to the evolution C_{ant}.

Ocean circulation, with vertical diffusion playing the largest role for short lived transient tracers, sets the time that it takes to reach this value. The mixed layer pulse response function must be calculated for each transient tracer of interest because the spatial distribution of flux is tracer dependent, thus each tracer flux distribution uniquely samples the spatially variable vertical diffusivity of the ocean. The mixed layer pulse response function for C_{ant} is determined by simulating the exposure of the surface ocean to a pulse of atmospheric CO_2 . In order to use a single case as our pulse response function, the size of the

https://doi.org/10.5194/bg-2020-254
Preprint. Discussion started: 16 July 2020

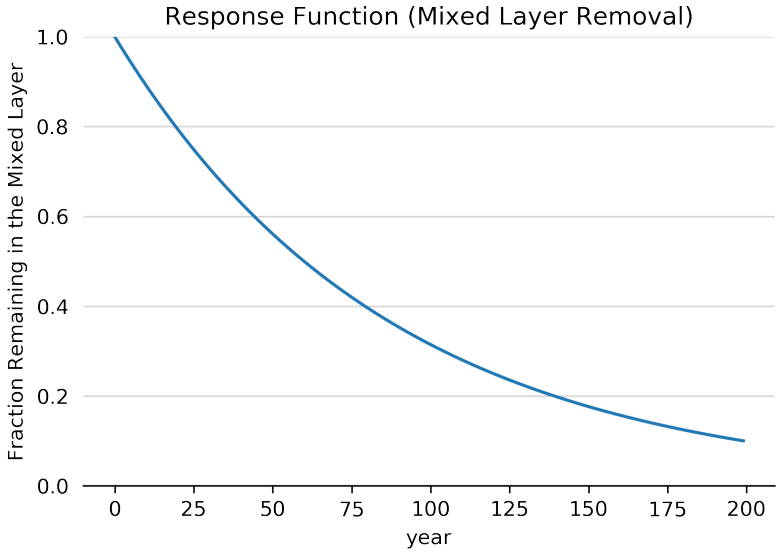

Figure A1. A conceptual example of the response function. This response function characterizes the decay of a transient tracer in the surface ocean.

pulse we give our model cannot affect the time it would take that pulse to reach 10%. In other words, the time it takes for any subsequent pulse to reach 10% in the mixed layer must also remain constant. In theory, the timescale could change as result of changes to ocean circulation, and as seen in the results this does occur, but minimally affects the response (Figure 2c).

One can use the convolution integral of the pulse and the response function to determine the surface ocean concentration of a transient tracer:

$$C_o(t) = \int_{t_i}^{t} F_c(u) r(t-u) du \tag{A1}$$

This is a slightly simplified version of the one-dimensional model equation, where C_o is the surface concentration of a tracer, F_c is the flux, and r is the response function. In our case, the pulse, F_c, is the change in carbon concentration at the surface each year. By taking the convolution integral of the pulse, and its response function, we can determine the change in mixed-layer concentration (Figure A2). A convolution integral (Equation A1) calculates the concentration at time t by calculating the fraction of previous pulses ($F_c(u)$), that entered the ocean at times u (from $t_i = 0$ to t), that remain in the surface ocean at time t. This is generalizable to any tracer that is initially absent in the ocean. An intuition for convolution integral can be formed by visualizing it in discrete form (Figure A2). By summing all of the discrete pulses that are present in the mixed layer at a given time, one can arrive at an approximation of the exact convolution integral (Figure A2c,d). In this case the exact solution is the ocean concentration of the transient tracer. In this generalized example, we show the effect of pulse sampling frequency (Figure A2c). With more frequent pulse sampling, the more accurate the approximation of the convolution integral (A2c,d),

https://doi.org/10.5194/bg-2020-254
Preprint. Discussion started: 16 July 2020

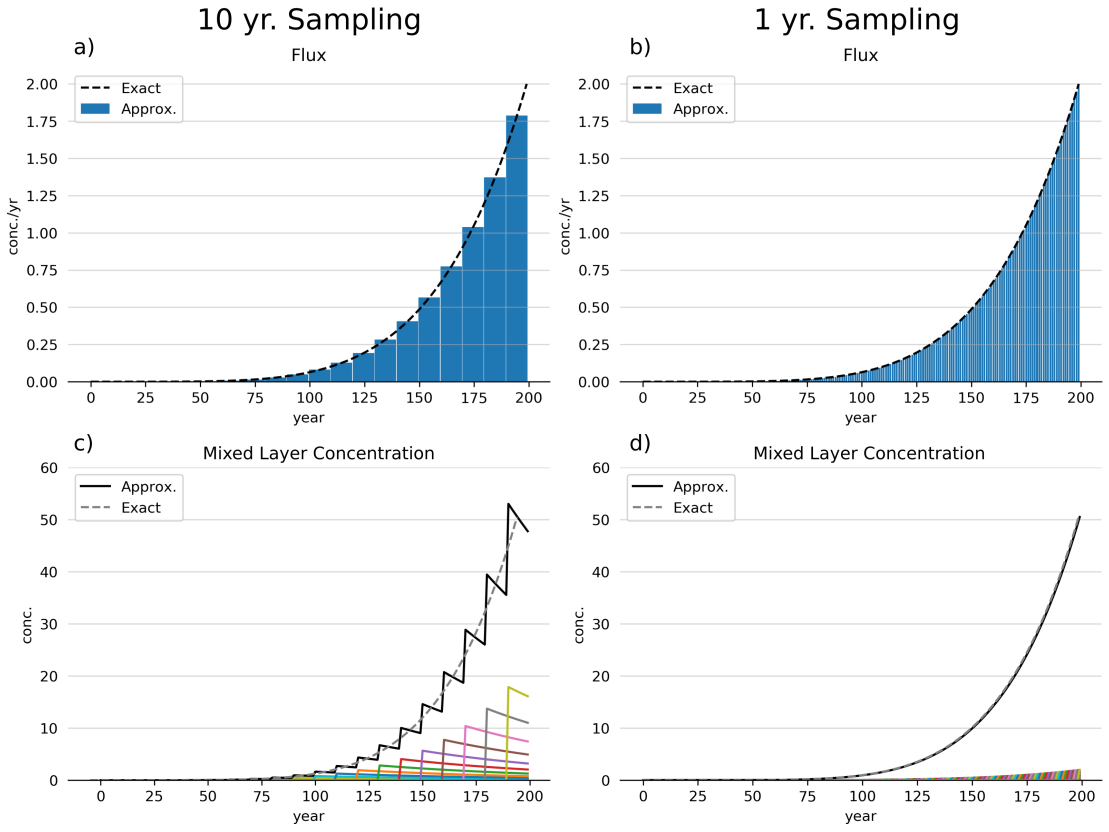

Figure A2. (a,b) Time series of the flux of transient tracer (concentration yr^{-1}), with different sampling frequencies shown with the blue bars. The left column is a 10 year sampling frequency, 1 year frequency in the right column. The blue bars are F_c in Equation A1. (c,d) Predicted transient tracer concentration in the surface ocean, the left hand-side of Equation A1. The predicted concentration (black line) at any point in time is the sum of the individual pulses at that time (colored lines).

thus with infinitely many pulses one can capture the full convolution integral (concentration of some transient tracer). In the one-dimensional model case, the pulse is sampled annually, with no benefit to sampling at sub-annual frequencies.

Interestingly, the convolution integral can be used to solve for the flux. All we need to know is the flux at $t = 0$. The flux of transient tracer can be described with the following equation:

$$F_C = \frac{k}{h}(C_{atm} - C_{ocn}) \tag{A2}$$

In this equation F_C is the flux of tracer in units of quantity (μmol, mol, kg, etc) per m^3. On the right hand side, the air-sea difference is multiplied by the gas transfer velocity, k (m yr^{-1}), and the mixed layer depth, h (m).

https://doi.org/10.5194/bg-2020-254
Preprint. Discussion started: 16 July 2020

We can calculate the initial flux of transient tracer with knowledge of the atmospheric history of the transient tracer, and also because by definition, we know the initial ocean concentration is 0. Beginning at $t = 0$, at each time step we can make these calculations in the following order to determine the flux for the entire period we have atmospheric measurements of the tracer:

1. Calculate the air-sea flux (Equation A2)
2. Sum up the pulses still present in the mixed layer to determine concentration at the next timestep (Equation A1).

This process is repeated to calculate the next year's air-sea flux. After many time steps, the flux is responding to the change in concentration that occurred in the previous year due to the previous year's flux, and any pulses that remain in the mixed layer.

Appendix B: One-Dimensional Ocean Carbon Cycle Model Chemistry

The pCO_2^{ocn} of the one-dimensional ocean carbon cycle model is calculated as follows:

$$pCO_2^{ocn} = [pCO_2^{ocn,PI} + \delta pCO_2^{ocn}(C_{ant}, T_0)]exp(\alpha_T \delta T) \tag{B1}$$

The response of pCO_2^{ocn} to warming is parameterized as an exponential function as in Takahashi et al. (1993), with α_T set to 0.0423 (Equation A24; Joos et al., 2001)). The δpCO_2^{ocn} is calculated using a fixed ocean alkalinity of 2300 μmol kg^{-1} and the preindustrial temperature, T_0. The chemistry of δpCO_2^{ocn} is parameterized as follows:

$$\delta pCO_2^{ocn}(C_{ant}, T_0) = C_{ant}[A1 + C_{ant}(A2 + C_{ant}(A3 + C_{ant}(A4 + C_{ant}A5)))] \tag{B2}$$

With coefficients:

$$A1 = (1.5568 - 1.3993 \times 10^{-2} \times T_0) \tag{B3}$$
$$A2 = (7.4706 - 0.20207 \times T_0) \times 10^{-3} \tag{B4}$$
$$A3 = -(1.2748 - 0.12015 \times T_0) \times 10^{-5} \tag{B5}$$
$$A4 = (2.4491 - 0.12639 \times T_0) \times 10^{-7} \tag{B6}$$
$$A5 = -(1.5468 - 0.15326 \times T_0) \times 10^{-10} \tag{B7}$$

Author contributions. Both authors contributed to the discussion and the writing of the paper

Competing interests. The authors declare that no competing interests are present

https://doi.org/10.5194/bg-2020-254
Preprint. Discussion started: 16 July 2020

Acknowledgements. We would like to thank Jared Lewis and Bodeker Scientific for sharing their pySCM (python Simple Climate Model, https://github.com/bodekerscientific/pyscm/) code on GitHub. This code provided the basis the one-dimensional ocean carbon cycle model presented here.

https://doi.org/10.5194/bg-2020-254
Preprint. Discussion started: 16 July 2020

References

Abernathey, R. P. and Marshall, J.: Global surface eddy diffusivities derived from satellite altimetry, Journal of Geophysical Research: Oceans, 118, 901–916, https://doi.org/10.1002/jgrc.20066, https://agupubs.onlinelibrary.wiley.com/doi/abs/10.1002/jgrc.20066, 2013.

Archer, D.: Fate of fossil fuel CO2 in geologic time, Journal of Geophysical Research: Oceans, 110, https://doi.org/10.1029/2004JC002625, https://agupubs.onlinelibrary.wiley.com/doi/abs/10.1029/2004JC002625, 2005.

Bopp, L., Lévy, M., Resplandy, L., and Sallée, J. B.: Pathways of anthropogenic carbon subduction in the global ocean, Geophysical Research Letters, 42, 6416–6423, https://doi.org/10.1002/2015GL065073, https://agupubs.onlinelibrary.wiley.com/doi/abs/10.1002/2015GL065073, 2015.

Canadell, J. G., Le Quéré, C., Raupach, M. R., Field, C. B., Buitenhuis, E. T., Ciais, P., Conway, T. J., Gillett, N. P., Houghton, R. A., and Marland, G.: Contributions to accelerating atmospheric CO2 growth from economic activity, carbon intensity, and efficiency of natural sinks, Proceedings of the National Academy of Sciences of the United States of America, 104, 18 866–18 870, https://doi.org/10.1073/pnas.0702737104, 2007.

Danabasoglu, G., Bates, S. C., Briegleb, B. P., Jayne, S. R., Jochum, M., Large, W. G., Peacock, S., and Yeager, S. G.: The CCSM4 Ocean Component, Journal of Climate, 25, 1361–1389, https://doi.org/10.1175/JCLI-D-11-00091.1, https://journals.ametsoc.org/doi/full/10.1175/JCLI-D-11-00091.1, 2011.

DeVries, T.: The oceanic anthropogenic CO2 sink: Storage, air-sea fluxes, and transports over the industrial era, Global Biogeochemical Cycles, 28, 631–647, https://doi.org/10.1002/2013GB004739, https://agupubs.onlinelibrary.wiley.com/doi/abs/10.1002/2013GB004739, 2014.

Dunne, J. P., John, J. G., Adcroft, A. J., Griffies, S. M., Hallberg, R. W., Shevliakova, E., Stouffer, R. J., Cooke, W., Dunne, K. A., Harrison, M. J., Krasting, J. P., Malyshev, S. L., Milly, P. C. D., Phillipps, P. J., Sentman, L. T., Samuels, B. L., Spelman, M. J., Winton, M., Wittenberg, A. T., and Zadeh, N.: GFDL's ESM2 Global Coupled Climate–Carbon Earth System Models. Part I: Physical Formulation and Baseline Simulation Characteristics, 25, 6646–6665, https://doi.org/10.1175/JCLI-D-11-00560.1, https://journals.ametsoc.org/jcli/article/25/19/6646/106194/GFDL-s-ESM2-Global-Coupled-Climate-Carbon-Earth, 2012.

Fassbender, A. J., Sabine, C. L., and Palevsky, H. I.: Nonuniform ocean acidification and attenuation of the ocean carbon sink, Geophysical Research Letters, 44, 8404–8413, https://doi.org/10.1002/2017GL074389, https://agupubs.onlinelibrary.wiley.com/doi/abs/10.1002/2017GL074389, 2017.

Friedlingstein, P., Meinshausen, M., Arora, V. K., Jones, C. D., Anav, A., Liddicoat, S. K., and Knutti, R.: Uncertainties in CMIP5 Climate Projections due to Carbon Cycle Feedbacks, Journal of Climate, 27, 511–526, https://doi.org/10.1175/JCLI-D-12-00579.1, https://journals.ametsoc.org/doi/full/10.1175/JCLI-D-12-00579.1, 2013.

Friedlingstein, P., Jones, M. W., O'Sullivan, M., Andrew, R. M., Hauck, J., Peters, G. P., Peters, W., Pongratz, J., Sitch, S., Quéré, C. L., Bakker, D. C. E., Canadell, J. G., Ciais, P., Jackson, R. B., Anthoni, P., Barbero, L., Bastos, A., Bastrikov, V., Becker, M., Bopp, L., Buitenhuis, E., Chandra, N., Chevallier, F., Chini, L. P., Currie, K. I., Feely, R. A., Gehlen, M., Gilfillan, D., Gkritzalis, T., Goll, D. S., Gruber, N., Gutekunst, S., Harris, I., Haverd, V., Houghton, R. A., Hurtt, G., Ilyina, T., Jain, A. K., Joetzjer, E., Kaplan, J. O., Kato, E., Klein Goldewijk, K., Korsbakken, J. I., Landschützer, P., Lauvset, S. K., Lefèvre, N., Lenton, A., Lienert, S., Lombardozzi, D., Marland, G., McGuire, P. C., Melton, J. R., Metzl, N., Munro, D. R., Nabel, J. E. M. S., Nakaoka, S.-I., Neill, C., Omar, A. M., Ono, T., Peregon, A., Pierrot, D., Poulter, B., Rehder, G., Resplandy, L., Robertson, E., Rödenbeck, C., Séférian, R., Schwinger, J., Smith, N., Tans, P. P., Tian,

https://doi.org/10.5194/bg-2020-254
Preprint. Discussion started: 16 July 2020

H., Tilbrook, B., Tubiello, F. N., Werf, G. R. v. d., Wiltshire, A. J., and Zaehle, S.: Global Carbon Budget 2019, Earth System Science Data, 11, 1783–1838, https://doi.org/https://doi.org/10.5194/essd-11-1783-2019, https://www.earth-syst-sci-data.net/11/1783/2019/, 2019.

Gammon, R. H., Cline, J., and Wisegarver, D.: Chlorofluoromethanes in the northeast Pacific Ocean: Measured vertical distributions and application as transient tracers of upper ocean mixing, Journal of Geophysical Research: Oceans, 87, 9441–9454, https://doi.org/10.1029/JC087iC12p09441, https://agupubs.onlinelibrary.wiley.com/doi/abs/10.1029/JC087iC12p09441, 1982.

Gent, P. R. and Mcwilliams, J. C.: Isopycnal Mixing in Ocean Circulation Models, Journal of Physical Oceanography, 20, 150–155, https://doi.org/10.1175/1520-0485(1990)020<0150:IMIOCM>2.0.CO;2, https://journals.ametsoc.org/doi/10.1175/1520-0485%281990%29020%3C0150%3AIMIOCM%3E2.0.CO%3B2, 1990.

Gnanadesikan, A., Pradal, M.-A., and Abernathey, R.: Isopycnal mixing by mesoscale eddies significantly impacts oceanic anthropogenic carbon uptake, Geophysical Research Letters, 42, 4249–4255, https://doi.org/10.1002/2015GL064100, https://agupubs.onlinelibrary.wiley.com/doi/abs/10.1002/2015GL064100, 2015.

Graven, H. D., Gruber, N., Key, R., Khatiwala, S., and Giraud, X.: Changing controls on oceanic radiocarbon: New insights on shallow-to-deep ocean exchange and anthropogenic CO2 uptake, Journal of Geophysical Research: Oceans, 117, https://doi.org/10.1029/2012JC008074, https://agupubs.onlinelibrary.wiley.com/doi/abs/10.1029/2012JC008074, 2012.

Gruber, N., Clement, D., Carter, B. R., Feely, R. A., Heuven, S. v., Hoppema, M., Ishii, M., Key, R. M., Kozyr, A., Lauvset, S. K., Monaco, C. L., Mathis, J. T., Murata, A., Olsen, A., Perez, F. F., Sabine, C. L., Tanhua, T., and Wanninkhof, R.: The oceanic sink for anthropogenic CO2 from 1994 to 2007, Science, 363, 1193–1199, https://doi.org/10.1126/science.aau5153, https://science.sciencemag.org/content/363/6432/1193, 2019a.

Gruber, N., Clement, D., Carter, B. R., Feely, R. A., van Heuven, S., Hoppema, M., Ishii, M., Key, R. M., Kozyr, A., Lauvset, S. K., Lo Monaco, C., Mathis, J. T., Murata, A., Olsen, A., Perez, F. F., Sabine, C. L., Tanhua, T., and Wanninkhof, R.: The oceanic sink for anthropogenic CO ₂ from 1994 to 2007, Science, https://doi.org/10.1126/science.aau5153, 2019b.

Jones, C., Robertson, E., Arora, V., Friedlingstein, P., Shevliakova, E., Bopp, L., Brovkin, V., Hajima, T., Kato, E., Kawamiya, M., Liddicoat, S., Lindsay, K., Reick, C. H., Roelandt, C., Segschneider, J., and Tjiputra, J.: Twenty-First-Century Compatible CO2 Emissions and Airborne Fraction Simulated by CMIP5 Earth System Models under Four Representative Concentration Pathways, Journal of Climate, 26, 4398–4413, https://doi.org/10.1175/JCLI-D-12-00554.1, https://journals.ametsoc.org/doi/full/10.1175/JCLI-D-12-00554.1, 2013.

Joos, F., Bruno, M., Fink, R., Siegenthaler, U., Stocker, T. F., Quéré, C. L., and Sarmiento, J. L.: An efficient and accurate representation of complex oceanic and biospheric models of anthropogenic carbon uptake, Tellus B, 48, 397–417, https://doi.org/10.1034/j.1600-0889.1996.t01-2-00006.x, https://onlinelibrary.wiley.com/doi/abs/10.1034/j.1600-0889.1996.t01-2-00006.x, 1996.

Joos, F., Prentice, I. C., Sitch, S., Meyer, R., Hooss, G., Plattner, G.-K., Gerber, S., and Hasselmann, K.: Global warming feedbacks on terrestrial carbon uptake under the Intergovernmental Panel on Climate Change (IPCC) Emission Scenarios, Global Biogeochemical Cycles, 15, 891–907, https://doi.org/10.1029/2000GB001375, https://agupubs.onlinelibrary.wiley.com/doi/abs/10.1029/2000GB001375, 2001.

Khatiwala, S., Primeau, F., and Hall, T.: Reconstruction of the history of anthropogenic CO 2 concentrations in the ocean, Nature, 462, 346–349, https://doi.org/10.1038/nature08526, https://www.nature.com/articles/nature08526, 2009.

Landschützer, P., Gruber, N., Haumann, F. A., Rödenbeck, C., Bakker, D. C. E., Heuven, S. v., Hoppema, M., Metzl, N., Sweeney, C., Takahashi, T., Tilbrook, B., and Wanninkhof, R.: The reinvigoration of the Southern Ocean carbon sink, Science, 349, 1221–1224, https://doi.org/10.1126/science.aab2620, https://science.sciencemag.org/content/349/6253/1221, 2015.

Large, W. G., McWilliams, J. C., and Doney, S. C.: Oceanic vertical mixing: A review and a model with a nonlocal boundary layer parameterization, Reviews of Geophysics, 32, 363–403, https://doi.org/10.1029/94RG01872, https://agupubs.onlinelibrary.wiley.com/doi/abs/10.1029/94RG01872, 1994.

Ledwell, J. R., Watson, A. J., and Law, C. S.: Mixing of a tracer in the pycnocline, 103, 21 499–21 529, https://doi.org/10.1029/98JC01738, https://agupubs.onlinelibrary.wiley.com/doi/abs/10.1029/98JC01738, 1998.

Lovenduski, N., Gruber, N., and Doney, S.: Toward a mechanistic understanding of the decadal trends in the Southern Ocean carbon sink, Global Biogeochem. Cycles, 22, https://doi.org/10.1029/2007GB003139, 2008.

McKinley, G. A., Fay, A. R., Eddebbar, Y. A., Gloege, L., and Lovenduski, N. S.: External Forcing Explains Recent Decadal Variability of the Ocean Carbon Sink, 1, e2019AV000 149, https://doi.org/10.1029/2019AV000149, https://agupubs.onlinelibrary.wiley.com/doi/abs/10.1029/2019AV000149, 2020.

Meinshausen, M., Smith, S. J., Calvin, K., Daniel, J. S., Kainuma, M. L. T., Lamarque, J.-F., Matsumoto, K., Montzka, S. A., Raper, S. C. B., Riahi, K., Thomson, A., Velders, G. J. M., and van Vuuren, D. P.: The RCP greenhouse gas concentrations and their extensions from 1765 to 2300, Climatic Change, 109, 213, https://doi.org/10.1007/s10584-011-0156-z, https://doi.org/10.1007/s10584-011-0156-z, 2011.

Moore, C. M., Mills, M. M., Arrigo, K. R., Berman-Frank, I., Bopp, L., Boyd, P. W., Galbraith, E. D., Geider, R. J., Guieu, C., Jaccard, S. L., Jickells, T. D., La Roche, J., Lenton, T. M., Mahowald, N. M., Marañón, E., Marinov, I., Moore, J. K., Nakatsuka, T., Oschlies, A., Saito, M. A., Thingstad, T. F., Tsuda, A., and Ulloa, O.: Processes and patterns of oceanic nutrient limitation, Nature Geoscience, 6, 701–710, https://doi.org/10.1038/ngeo1765, https://www.nature.com/articles/ngeo1765, 2013.

Oeschger, H., Siegenthaler, U., Schotterer, U., and Gugelmann, A.: A box diffusion model to study the carbon dioxide exchange in nature, Tellus, 27, 168–192, https://doi.org/10.1111/j.2153-3490.1975.tb01671.x, https://onlinelibrary.wiley.com/doi/abs/10.1111/j.2153-3490.1975.tb01671.x, 1975.

Peters, G. P., Le Quéré, C., Andrew, R. M., Canadell, J. G., Friedlingstein, P., Ilyina, T., Jackson, R. B., Joos, F., Korsbakken, J. I., McKinley, G. A., Sitch, S., and Tans, P.: Towards real-time verification of CO 2 emissions, Nature Climate Change, 7, 848–850, https://doi.org/10.1038/s41558-017-0013-9, https://www.nature.com/articles/s41558-017-0013-9, 2017.

Randerson, J., Lindsay, K., Munoz, E., Fu, W., Moore, J., Hoffman, F., Mahowald, N., and Doney, S.: Multicentury changes in ocean and land contributions to the climate-carbon feedback: CARBON CYCLE FEEDBACKS TO 2300 IN CESM, Global Biogeochemical Cycles, 29, https://doi.org/10.1002/2014GB005079, 2015.

Raupach, M. R., Gloor, M., Sarmiento, J. L., Canadell, J. G., Frölicher, T. L., Gasser, T., Houghton, R. A., Le Quéré, C., and Trudinger, C. M.: The declining uptake rate of atmospheric CO_2 by land and ocean sinks, Biogeosciences, 11, 3453–3475, https://doi.org/10.5194/bg-11-3453-2014, https://www.biogeosciences.net/11/3453/2014/, 2014.

Redi, M. H.: Oceanic Isopycnal Mixing by Coordinate Rotation, Journal of Physical Oceanography, 12, 1154–1158, https://doi.org/10.1175/1520-0485(1982)012<1154:OIMBCR>2.0.CO;2, https://journals.ametsoc.org/doi/abs/10.1175/1520-0485%281982%29012%3C1154%3AOIMBCR%3E2.0.CO%3B2, 1982.

Rogelj, J., Popp, A., Calvin, K. V., Luderer, G., Emmerling, J., Gernaat, D., Fujimori, S., Strefler, J., Hasegawa, T., Marangoni, G., Krey, V., Kriegler, E., Riahi, K., van Vuuren, D. P., Doelman, J., Drouet, L., Edmonds, J., Fricko, O., Harmsen, M., Havlík, P., Humpenöder, F., Stehfest, E., and Tavoni, M.: Scenarios towards limiting global mean temperature increase below 1.5 °C, Nature Climate Change, 8, 325–332, https://doi.org/10.1038/s41558-018-0091-3, https://www.nature.com/articles/s41558-018-0091-3, 2018.

https://doi.org/10.5194/bg-2020-254
Preprint. Discussion started: 16 July 2020

Sanderson, B. M., Xu, Y., Tebaldi, C., Wehner, M., O'Neill, B., Jahn, A., Pendergrass, A. G., Lehner, F., Strand, W. G., Lin, L., Knutti, R., and Lamarque, J. F.: Community climate simulations to assess avoided impacts in 1.5 and 2 °C futures, Earth System Dynamics, 8, 827–847, https://doi.org/https://doi.org/10.5194/esd-8-827-2017, https://www.earth-syst-dynam.net/8/827/2017/, 2017.

Sarmiento, J. L. and LeQuéré, C.: Oceanic Carbon Dioxide Uptake in a Model of Century-Scale Global Warming, Science, 274, 1346–1350, https://doi.org/10.1126/science.274.5291.1346, https://science.sciencemag.org/content/274/5291/1346, 1996.

Schwinger, J. and Tjiputra, J.: Ocean Carbon Cycle Feedbacks Under Negative Emissions, Geophysical Research Letters, 45, 5062–5070, https://doi.org/10.1029/2018GL077790, https://agupubs.onlinelibrary.wiley.com/doi/abs/10.1029/2018GL077790, 2018.

Takahashi, T., Sutherland, S. C., Wanninkhof, R., Sweeney, C., Feely, R. A., Chipman, D. W., Hales, B., Friederich, G., Chavez, F., Sabine, C., Watson, A., Bakker, D. C., Schuster, U., Metzl, N., Yoshikawa-Inoue, H., Ishii, M., Midorikawa, T., Nojiri, Y., Körtzinger, A., Steinhoff, T., Hoppema, M., Olafsson, J., Arnarson, T. S., Tilbrook, B., Johannessen, T., Olsen, A., Bellerby, R., Wong, C. S., Delille, B., Bates, N. R., and de Baar, H. J.: Climatological mean and decadal change in surface ocean pCO2, and net sea-air CO2 flux over the global oceans, Deep-Sea Research Part II: Topical Studies in Oceanography, https://doi.org/10.1016/j.dsr2.2008.12.009, 2009.

Tanhua, T., Körtzinger, A., Friis, K., Waugh, D. W., and Wallace, D. W. R.: An estimate of anthropogenic CO2 inventory from decadal changes in oceanic carbon content, 104, 3037–3042, https://doi.org/10.1073/pnas.0606574104, https://www.pnas.org/content/104/9/3037, 2007.

Tokarska, K. B., Zickfeld, K., and Rogelj, J.: Path Independence of Carbon Budgets When Meeting a Stringent Global Mean Temperature Target After an Overshoot, 7, 1283–1295, https://doi.org/10.1029/2019EF001312, https://agupubs.onlinelibrary.wiley.com/doi/abs/10.1029/2019EF001312.

Toyama, K., Rodgers, K. B., Blanke, B., Iudicone, D., Ishii, M., Aumont, O., and Sarmiento, J. L.: Large Reemergence of Anthropogenic Carbon into the Ocean's Surface Mixed Layer Sustained by the Ocean's Overturning Circulation, Journal of Climate, 30, 8615–8631, https://doi.org/10.1175/JCLI-D-16-0725.1, https://journals.ametsoc.org/doi/full/10.1175/JCLI-D-16-0725.1, 2017.

UNEP: Emissions Gap Report 2018, http://www.unenvironment.org/resources/emissions-gap-report-2018, 2018.

van Vuuren, D. P., Edmonds, J., Kainuma, M., Riahi, K., Thomson, A., Hibbard, K., Hurtt, G. C., Kram, T., Krey, V., Lamarque, J.-F., Masui, T., Meinshausen, M., Nakicenovic, N., Smith, S. J., and Rose, S. K.: The representative concentration pathways: an overview, Climatic Change, 109, 5, https://doi.org/10.1007/s10584-011-0148-z, https://doi.org/10.1007/s10584-011-0148-z, 2011.

Zickfeld, K., Macdougall, A. H., and Matthews, H. D.: On the proportionality between global temperature change and cumulative CO 2 emissions during periods of net negative CO 2 emissions, Environmental Research Letters, 11, 055 006, https://doi.org/10.1088/1748-9326/11/5/055006, 2016.